Monthly Notices
of the
ROYAL ASTRONOMICAL SOCIETY

MNRAS **456,** 3194–3211 (2016) doi:10.1093/mnras/stv2857

The galaxy UV luminosity function at $z \simeq 2$–4; new results on faint-end slope and the evolution of luminosity density

Shaghayegh Parsa,★ James S. Dunlop,★ Ross J. McLure and Alice Mortlock
Institute for Astronomy, University of Edinburgh, Royal Observatory, Edinburgh, EH9 3HJ, UK

Accepted 2015 December 2. Received 2015 November 2; in original form 2015 July 20

ABSTRACT

We present a new, robust measurement of the evolving rest-frame ultraviolet (UV) galaxy luminosity function (LF) over the key redshift range from $z \simeq 2$ to $z \simeq 4$. Our results are based on the high dynamic range provided by combining the *Hubble Ultra Deep Field* (*HUDF*), CANDELS/GOODS-South, and UltraVISTA/COSMOS surveys. We utilize the unparalleled multifrequency photometry available in this survey 'wedding cake' to compile complete galaxy samples at $z \simeq 2$, 3, 4 via photometric redshifts (calibrated against the latest spectroscopy) rather than colour–colour selection, and to determine accurate rest-frame UV absolute magnitudes (M_{1500}) from spectral energy distribution (SED) fitting. Our new determinations of the UV LF extend from $M_{1500} \simeq -22$ (AB mag) down to $M_{1500} = -14.5$, -15.5 and -16 at $z \simeq 2$, 3 and 4, respectively (thus, reaching $\simeq 3$–4 mag fainter than previous blank-field studies at $z \simeq 2$,3). At $z \simeq 2$, 3, we find a much shallower faint-end slope ($\alpha = -1.32 \pm 0.03$) than reported in some previous studies ($\alpha \simeq -1.7$), and demonstrate that this new measurement is robust. By $z \simeq 4$, the faint-end slope has steepened slightly, to $\alpha = -1.43 \pm 0.04$, and we show that these measurements are consistent with the overall evolutionary trend from $z = 0$ to 8. Finally, we find that while characteristic number density (ϕ^*) drops from $z \simeq 2$ to $z \simeq 4$, characteristic luminosity (M^*) brightens by $\simeq 1$ mag. This, combined with the new flatter faint-end slopes, has the consequence that UV luminosity density (and hence unobscured star formation density) peaks at $z \simeq 2.5$–3, when the Universe was $\simeq 2.5$ Gyr old.

Key words: galaxies: evolution – galaxies: luminosity function, mass function – galaxies: photometry.

1 INTRODUCTION

Ultraviolet (UV) continuum emission provides the most direct tracer of star formation activity in a galaxy (e.g. Kennicutt & Evans 2012), albeit it must be corrected for the impact of dust obscuration to derive complete star formation rates (SFR). This, coupled with the easy access to the rest-frame UV regime ($\lambda = 1500$–1700 Å) provided by optical observations of galaxies at redshifts $z \gtrsim 1.5$, has meant that the determination of the evolving UV galaxy luminosity function (LF) has become a key probe of galaxy evolution and overall cosmic star formation history (e.g. Bouwens et al. 2007; Reddy & Steidel 2009; Robertson et al. 2010; McLure et al. 2013; Madau & Dickinson 2014).

All evidence to date, as provided by a wide range of studies discussed later in this paper, indicates that, at redshifts $z \simeq 2$–6, the UV LF is well described by a Schechter function (Schechter 1976). However, as with all LF studies, the challenge is to assemble galaxy samples of adequate size, spanning a large enough dynamic range, and with sufficiently accurate/complete redshift information to robustly determine both the bright and faint end of the LF. Thus, ideally, large-area surveys are required to adequately sample the bright end of the LF (and mitigate the impact of cosmic variance) while very deep, small-area surveys are necessary to yield the data required to properly constrain the faint-end slope, α. This latter quantity is of particular importance if it is hoped to perform a reliable luminosity-weighted integral of the LF down to faint magnitude limits to determine UV luminosity density ($\rho_{\rm UV}$). In practice, galaxy selection is also a key issue, and it is particularly important to understand sample completeness as a function of magnitude and redshift, especially if simple colour–colour selection techniques are utilized to select samples of UV luminous star-forming galaxies.

After the early pioneering studies of UV luminosity density indicated it was rising with lookback time out to at least $z \simeq 1.5$ (e.g. Lilly et al. 1996; Madau et al. 1996; Arnouts et al. 2005), the first detailed study of the galaxy UV LF at $z \simeq 2$–3 was attempted by Reddy & Steidel (2009). This work was based on colour selection of galaxies from ground-based data, and as such was best suited to determining the bright end of the LF at $M_{\rm UV} < -18$ (AB mag). None the less, a key result of this paper was the derivation of an

★ E-mail: shp@roe.ac.uk (SP); jsd@roe.ac.uk (JSD)

extremely steep-faint slope for the UV LF at these intermediate redshifts, with $\alpha = -1.73 \pm 0.07$. This result appears to have been confirmed by subsequent, deeper, *Hubble Space Telescope* (*HST*) studies following the installation of WFC3 in 2009; first Oesch et al. (2010) reported that $\alpha = -1.60 \pm 0.21$ at $z \simeq 1.7$, and then, very recently, Alavi et al. (2014) used WFC3/UVIS combined with the gravitational lensing boost provided by the cluster A1689 to probe the UV LF at $z \simeq 2$ down to (lensing corrected) magnitudes $M_{1500} \simeq -13$, yielding $\alpha = -1.74 \pm 0.08$.

However, there has not been universal agreement; for example, Hathi et al. (2010) reported that $\alpha = -1.17 \pm 0.40$ at $z \simeq 2.1$, and Sawicki (2012) found $\alpha = -1.47 \pm 0.24$ at $z \simeq 2$. In addition, Weisz, Johnson & Conroy (2014) have recently used galactic archaeology techniques to 'reverse engineer' the stellar populations found in the present-day Local Group galaxy population, and conclude in favour of $\alpha = -1.35 \pm 0.12$ at $z = 2$–3.

Such results are interesting, but this controversy simply reinforces the importance of undertaking a new, direct investigation of the UV LF at this key epoch in cosmic history. Moreover, a new measurement of the UV LF at $z = 2$–4 is timely, given the huge recent improvement in the necessary multifrequency imaging (and supporting spectroscopy) in key deep *HST and* ground-based survey fields.

In this study we have exploited the combined power of the latest optical–infrared data in the *Hubble Ultra Deep Field* (*HUDF*) (reaching $\simeq$29.5 mag over 4.5 arcmin^2), the CANDELS/GOODS-S field (reaching $\simeq$27.5 mag over 170 arcmin^2), and the UltraVISTA/COSMOS field (reaching $\simeq$26 mag over $\simeq$0.5 deg^2). In recent years, driven by the rapid improvements in the near-infrared depth arising from the advent of WFC3/IR and VISTA imaging (e.g. Grogin et al. 2011; McCracken et al. 2012; Koekemoer et al. 2013) the unparalleled data in these key fields have been very actively exploited in the study of the UV LF at higher redshifts, $z = 5$–8 (e.g. McLure et al. 2010, 2013; Oesch et al. 2010, 2013; Finkelstein et al. 2010, 2015; Bouwens et al. 2011, 2015; Bowler et al. 2014, 2015). However, the full multifrequency data sets have not recently been properly applied to revisit the measurement of the UV LF in the redshift range $z = 2$–4. Our new study thus aims to rectify this situation, and to also take advantage of new optical and near-infrared spectroscopy (including WFC3/IR grism spectroscopy; Skelton et al. 2014; Morris et al. 2015) to help produce the most reliable photometric redshifts (crucial both for robust galaxy sample selection, and for the accurate determination of M_{1500} or M_{1700} for each source).

The remainder of this paper is structured as follows. In Section 2, we summarize the available imaging/photometric data for our three-tier 'wedding-cake' survey. Next, in Section 3, we summarize the available spectrosocopic data, and explain how we have used robust photometric redshift estimation to assemble a combined sample of $\simeq$ 35 000 galaxies in the redshift range of interest, $1.5 < z < 4.5$. We then proceed, in Section 4, to analyse the resulting galaxy data set to derive the UV LF, focusing first on the detailed shape (especially the faint-end slope, α) of the LF at $z \simeq 2$, and then expanding the analysis up to $z \simeq 4$. In Section 5, we compare our results to those of other authors, place our findings in the context of published results on the evolution of the UV LF up to $z \simeq 8$, and discuss the implications of our derived UV luminosity density, $\rho_{\rm UV}$, over the redshift range $z = 2$–4. Our conclusions are summarized in Section 6.

Throughout, we assume that a flat cosmology with $\Omega_0 = 0.3$, $\Omega_\Lambda = 0.7$ and $H_0 = 70$ kms^{-1}Mpc^{-1}, and give all magnitudes in the AB system (Oke 1974; Oke & Gunn 1983).

Table 1. A summary of the photometry used in this study, giving the 5σ detection limits in each filter/field as appropriate. The filter names are as summarized at the beginning of Section 2. For the *HST* photometry, the depths given refer to total magnitudes, as derived from small-aperture magnitudes assuming point-source corrections (see McLure et al. 2013). The *Spitzer* IRAC depths also refer to total magnitudes, as derived using TPHOT (Merlin et al. 2015). The depths for the ground-based photometry are based on two-arcsec diameter aperture measurements.

Filter	Survey		
	HUDF	CANDELS/ GOODS-S	UltraVISTA/ COSMOS
U	28.0	28.0	
u			27.0
B_{435}	29.7	28.0	
g			27.1
V_{606}	30.2	28.4	
r			26.6
i_{775}	29.9	27.8	
i'			26.3
i_{814}	29.8		
z'			25.4
z			26.4
z_{850}	29.1	27.5	
Y_{105}	29.7	27.9	
Y			25.1
J_{125}	29.2	27.7	
J			24.9
J_{140}	29.2		
H_{160}	29.2	27.3	
H			24.6
$K_{\rm s}$	26.5	26.5	24.8
$IRAC_{3.6}$	26.5	26.5	25.2
$IRAC_{4.8}$	26.3	26.3	25.2

2 IMAGING DATA AND PHOTOMETRY

In this section, we summarize the properties of the three surveys used in this study, and explain how the galaxies were selected, and their multifrequency photometry measured.

Throughout, we refer to the *HST* ACS and WFC3/IR filters *F*435*W*, *F*606*W*, *F*775*W*, *F*814*W*, *F*850*LP*, *F*098*M*, *F*105*W*, *F*125*W*, *F*140*W* and *F*160*W* as B_{435}, V_{606}, i_{775}, i_{814}, z_{850}, Y_{098}, Y_{105}, J_{125}, J_{140} and H_{160}, respectively, the VLT VIMOS-U and Hawk-I/K-215 filters as U and $K_{\rm s}$, respectively, the CFHT MegaCam optical filters as u, g, r, i', z', the reddest Subaru Suprime-Cam filter as z, the four broad-band VISTA near-infrared filters as Y, J, H and $K_{\rm s}$, and the *Spitzer* IRAC first two channels as $IRAC_{3.6\,\mu{\rm m}}$ and $IRAC_{4.5\,\mu{\rm m}}$.

The photometric depths of the imaging data in each filter, for each field, are summarized for convenience in Table 1, with further details for each field given in the following subsections.

2.1 *Hubble Ultra Deep Field*

The deepest data set we analyse, which is crucial for constraining the faint end of the galaxy UV LF, is the multiband imaging of the *Hubble Ultra Deep Field* completed in 2012 (*HUDF*12), covering an area of $\simeq$4.5 arcmin^2. This latest comprehensive data set consists of the deepest near-infrared imaging obtained with *HST* WFC3/IR from the *HUDF*09 and *HUDF*12 programmes (Bouwens et al. 2010; Ellis et al. 2013; Koekemoer et al. 2013), and the original optical *HST* ACS imaging (Beckwith et al. 2006) supplemented by new deep i_{814} imaging. To maximize wavelength coverage, we have supplemented the *HST* data with the public VLT GOODS-S U

imaging (Nonino et al. 2009), the Hawk-I K_s imaging from the HUGS programme (Fontana et al. 2014), and the deepest available IRAC imaging (McLure et al. 2011; Ashby et al. 2013).

Galaxy detection and photometry from this deep *HST* imaging data set was undertaken using SEXTRACTOR v2.8.6 (Bertin & Arnouts 1996) in dual-image mode with H_{160} as the detection image and the FLUX-ISO as the observed isophotal flux. In order to obtain consistent resolution-matched photometry, the lower resolution U, K_s and IRAC images were deconfused using the technique described in McLure et al. (2011).

Our final photometric catalogue for the *HUDF* includes the photometry of 2864 sources with $H_{160} < 29.5$, measured in the U, B_{435}, V_{606}, i_{775}, i_{814}, z_{850}, Y_{105}, J_{125}, J_{140}, H_{160}, K_s, $IRAC_{3.6\,\mu m}$ and $IRAC_{4.5\,\mu m}$ bands.

2.2 CANDELS/GOODS-S

To provide the next tier of the survey 'wedding cake', we have used the publicly-available *HST* WFC3/IR and *HST* ACS imaging of the Great Observatories Origins Deep Survey South (GOODS-S) field provided by the Cosmic Assembly Near-Infrared Deep Extragalactic Legacy Survey (CANDELS) (Grogin et al. 2011; Koekemoer et al. 2011; Windhorst et al. 2011), and the associated pre-existing *HST* optical (Giavalisco et al. 2004; Riess et al. 2007), ground-based VLT U band (Nonino et al. 2009) and K_s band (Retzlaff et al. 2010; Fontana et al. 2014), and *Spitzer* IRAC imaging (Ashby et al. 2013), as summarized by Guo et al. (2013).

Consistent with the production of the *HUDF* catalogue, the sources were detected, and their isophotal fluxes in the *HST* bands measured using SEXTRACTOR v2.8.6 (Bertin & Arnouts 1996) in dual-image mode, again with H_{160} as the detection image. As described in Guo et al. (2013), in this field the Template FITting (TFIT) method (Laidler et al. 2007) has been applied to generate the matched photometry from the lower angular resolution U, K_s and IRAC imaging. The GOODS-S catalogue provided by Guo et al. (2013) contains 34 930 sources in an area of 173 arcmin^2, with photometry in the U, B_{435}, V_{606}, i_{775}, z_{850}, Y_{098}, Y_{105}, J_{125}, H_{160}, K_s, $IRAC_{3.6\,\mu m}$ and $IRAC_{4.5\,\mu m}$ bands.

2.3 UltraVISTA/COSMOS

Data Release 2 (DR2) of the UltraVISTA survey (McCracken et al. 2012) provides deep near-infrared imaging in four deep strips which overlap $\simeq$0.7 deg^2 of the area also covered by the *HST* imaging of the Cosmological Evolution Survey (COSMOS; Scoville et al. 2007), and by the Canada–France–Hawaii Telescope Legacy Survey (CFHTLS) MegaCam deep optical imaging. As discussed in Bowler et al. (2012, 2014, 2015), for the central square degree covered by the CFHTLS D2 imaging, very deep Subaru Suprime-Cam z-band imaging has also been obtained (Furusawa et al., in preparation).

The photometry of the sources in the UltraVISTA+COSMOS imaging has been measured in 2 arcsec diameter apertures using SEXTRACTOR in dual-image mode. The detection image used in this case is the i'-band image from the T0007 release of the CFHTLS. These fluxes have been converted to total using the i'-band FLUX_AUTO parameter, and in this case the new TPHOT code (Merlin et al. 2015) has been used to obtain deconfused, resolution-matched IRAC fluxes.

The final UltraVISTA+COSMOS catalogue utilized, here, contains 89 614 galaxies with $i' < 26$, selected from an area of 0.482 deg^2 (reduced to an effective survey area of 0.292 deg^2 after masking for bright objects, and diffraction spikes etc), and provides photometry in the u, g, r, i' and z' bands from the CFHTLS, the z band from Suprime-Cam on Subaru, the Y, J, H, and K_s bands from UltraVISTA, and deconfused $IRAC_{3.6\,\mu m}$ and $IRAC_{4.5\,\mu m}$ photometry from a combination of the *Spitzer* Extended Deep Survey (SEDS; PI: Fazio; Ashby et al. 2013) and the *Spitzer* Large Area Survey with Hyper-SuprimeCam (SPLASH; PI: Capak).

3 REDSHIFT INFORMATION

In an ideal world, the galaxy LFs would be derived from large, complete, galaxy samples with complete spectroscopic redshift information. However, at the depths of interest here, even semi-complete spectroscopic redshift information is clearly (currently) not possible. Consequently, the robustness of our final results depends crucially on the reliability and accuracy of photometric redshifts derived for the galaxies uncovered for each of the three survey fields discussed above.

To test/optimize the derived photometric redshifts, subsets of objects with reliable spectroscopic redshifts are required. We have therefore assembled the latest catalogues of robust spectroscopic redshifts in the *HUDF*, GOODS-S and COSMOS fields. The results of this search are summarized in the first subsection below.

We then explain the steps taken to optimize photometric redshifts, the final procedure adopted, and quantify the reliability and accuracy of our final photometric redshifts via comparison with the spectroscopic data base (with further details and comparisons with other published photometric redshift catalogues given in Appendix A).

In the third subsection below, we describe our final combined sample of galaxies with redshifts in the range $1.5 < z < 4.5$. This sample is used in the LF analyses presented in the remainder of this paper.

3.1 Spectroscopic redshifts

Despite the fact that the *HUDF*, GOODS-S and COSMOS fields have been targeted by several of the most dense and deep spectrosopic surveys ever undertaken, typically at most $\simeq$ 10 per cent of the galaxies in our photometric samples possess high-quality spectroscopic redshifts. None the less, spectroscopic redshift information is crucial for refining and quantifying the accuracy (e.g. σ) and reliability (e.g. number of catastrophic outliers) of photometric redshifts.

We have therefore assembled catalogues including the very latest spectroscopic redshift information in each field. Within the GOODS-S field (including the *HUDF*), we have assembled a sample of 2799 galaxies with high-quality redshifts (218 of which lie within the area covered by the WFC3/IR imaging of the *HUDF*). We have confined our selection to only the very highest quality flags assigned to the redshifts obtained by each study in the literature, and the resulting redshift distribution of our final spectroscopic galaxy subsample (after removal of any stars or AGN) is shown in Fig. 1. As illustrated by the blue histogram in Fig. 1, the majority of this spectroscopic redshift information (1917 redshifts) has been obtained from ground-based optical spectroscopy (Cristiani et al. 2000; Croom, Warren & Glazebrook 2001; Le Févre et al. 2004; Strolger et al. 2004; Szokoly et al. 2004; Doherty et al. 2005; Mignoli et al. 2005; Roche et al. 2006; Cimatti et al. 2008; Vanzella et al. 2008; Balestra et al. 2010; Silverman et al. 2010). However, as illustrated by the red histogram in Fig. 1, it can also been seen that recent *HST* WFC3/IR near-infrared grism spectroscopy (Skelton

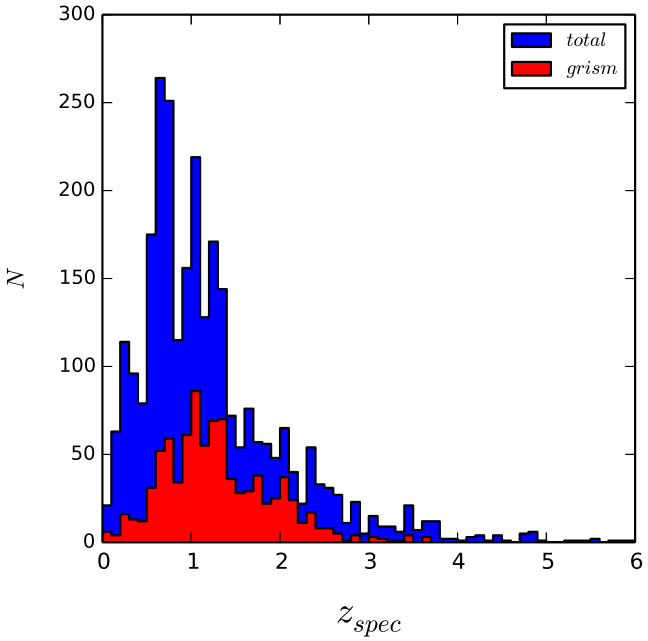

Figure 1. The distribution of the 2799 high-quality spectroscopic redshifts in the latest spectroscopic sample we have assembled for the CANDELS/GOODS-S field. The red histogram indicates the new WFC3/IR near-infrared grism redshifts as determined by the 3D-*HST* survey (Skelton et al. 2014) and CANDELS (Morris et al. 2015), which have helped significantly to fill in the 'redshift desert'. Of the 2799 objects with high-quality spectroscopic redshifts shown here, 218 lie within the *HUDF*.

et al. 2014; Morris et al. 2015) has now made an important contribution to the redshift coverage in this deep field (982 redshifts), in particular helping to fill in the traditional 'redshift desert' between $z \simeq 1.2$ and $z \simeq 2$, where relatively few strong emission lines are accessible in the optical regime.

Within the COSMOS field, we utilized a sample of 1877 high-quality redshifts as provided by the public z-COSMOS survey (Lilly et al. 2007).

3.2 Photometric redshifts

3.2.1 Method

To determine photometric redshifts, we used the public galaxy template-fitting code LE PHARE[1] (PHotometric Analysis for Redshift Estimate; Ilbert et al. 2006). To ensure the proper treatment of weak/non-detections, we fitted in flux-density rather than magnitude space. To account for dust obscuration/reddening, we assumed the dust-attenuation law of Calzetti et al. (2000), allowing reddening to vary over the range $0.0 < E(B-V) < 0.5$ in steps of $\Delta E(B-V) = 0.1$. We also included IGM absorption assuming the models of Madau (1995).

For each field, we proceeded in four stages. First, to avoid too much weight being placed on individual photometric detections, and to allow for remaining low-level systematic errors, we set a minimum of error of 3 per cent on all optical and near-infrared photometry, and a minimum error of 10 per cent on all IRAC photometry. Next, we utilized the galaxy SED templates provided by the evolutionary synthesis models of Bruzual & Charlot (2003) (BC03), without emission lines, and adjusted the photometric zero-points until the accuracy of the photometric redshifts was maximized (as judged by comparison with the high-quality spectroscopic redshifts discussed above). After this, we explored the use of a range of different galaxy templates, before determining that the PEGASEV2.0 models (Fioc & Rocca-Volmerange 1999), with emission lines switched on, produced the most accurate final photometric redshifts. Finally, we determined the photometric redshift for each galaxy by searching the redshift range $z = 0$–10, and distinguished between acceptable and unacceptable photometric redshifts based on an analysis of the distribution of minimum χ^2 (resulting in the acceptance of final SED fits with minimum $\chi^2 < 50$ in the fields with *HST* photometry, and minimum $\chi^2 < 20$ in the UltraVISTA/COSMOS field). This level of quality control led to the exclusion of <5 per cent of galaxies in the photometric samples from the final sample with trusted photometric redshifts.

Below, we summarize the results obtained in each field.

3.2.2 HUDF photometric redshifts

As outlined above, we refined the *HUDF* photometric zero-points by fitting the photometry with the BC03 models; the derived zero-point offsets were all smaller than 0.1 mag. After application of LE PHARE with emission lines, we derived acceptable ($\chi^2 < 50$) photometric redshifts for 2730 galaxies with $H < 29.5$ in the *HUDF*.

The accuracy of the derived photometric redshifts in the *HUDF* is illustrated in the top panel of Fig. 2, which shows $z_{\rm phot}$ v $z_{\rm spec}$ for the 210 sources in the field with secure spectroscopic redshifts, *and* acceptable photometric redshifts. The outlier fraction is 4.2 per cent, and $\sigma_{\rm NMAD} = 0.026$. For redshifts confined to $z > 1.5$ the $z_{\rm phot}$ v $z_{\rm spec}$ plot is shown in the top panel of Fig. 3 (see Appendix A for further details).

3.2.3 CANDELS/GOODS-S photometric redshifts

To maximize the reliability of the photometric redshifts for this sample, we confined our attention to sources with $H_{160} < 26$ in the CANDELS Wide region, and to sources with $H_{160} < 27$ in the CANDELS Deep region (which covers the central $\simeq 55$ arcmin^2 of GOODS-S), and then again refined the photometric zero-points by fitting the photometry with the BC03 models; the derived zero-point offsets were again all smaller than 0.1 mag.

After application of LE PHARE with emission lines, we derived acceptable ($\chi^2 < 50$) photometric redshifts for 10 987 galaxies with $H < 27$ in the GOODS-S Deep field, and for 27 460 galaxies with $H < 26$ in the GOODS-S Wide field.

The accuracy of the derived photometric redshifts in CANDELS/GOODS-S is illustrated in the middle panel of Fig. 2, which shows $z_{\rm phot}$ v $z_{\rm spec}$ for the 2677 sources in the field with secure spectroscopic redshifts, *and* acceptable photometric redshifts. The outlier fraction is 3 per cent, and $\sigma_{\rm NMAD} = 0.027$. For redshifts confined to $z > 1.5$ the $z_{\rm phot}$ v $z_{\rm spec}$, plot is shown in the middle panel of Fig. 3 (see Appendix A for further details).

3.2.4 UltraVISTA/COSMOS photometric redshifts

As with the *HST*-based catalogues, initially the photometric redshifts were computed by fitting the ground-based and *Spitzer* photometry to the BC03 models, in order to adjust the photometric zero-points until maximum redshift accuracy was achieved; all the derived zero-point offsets were again all smaller than 0.1 mag.

[1] http://www.cfht.hawaii.edu/arnouts/LEPHARE/lephare.html

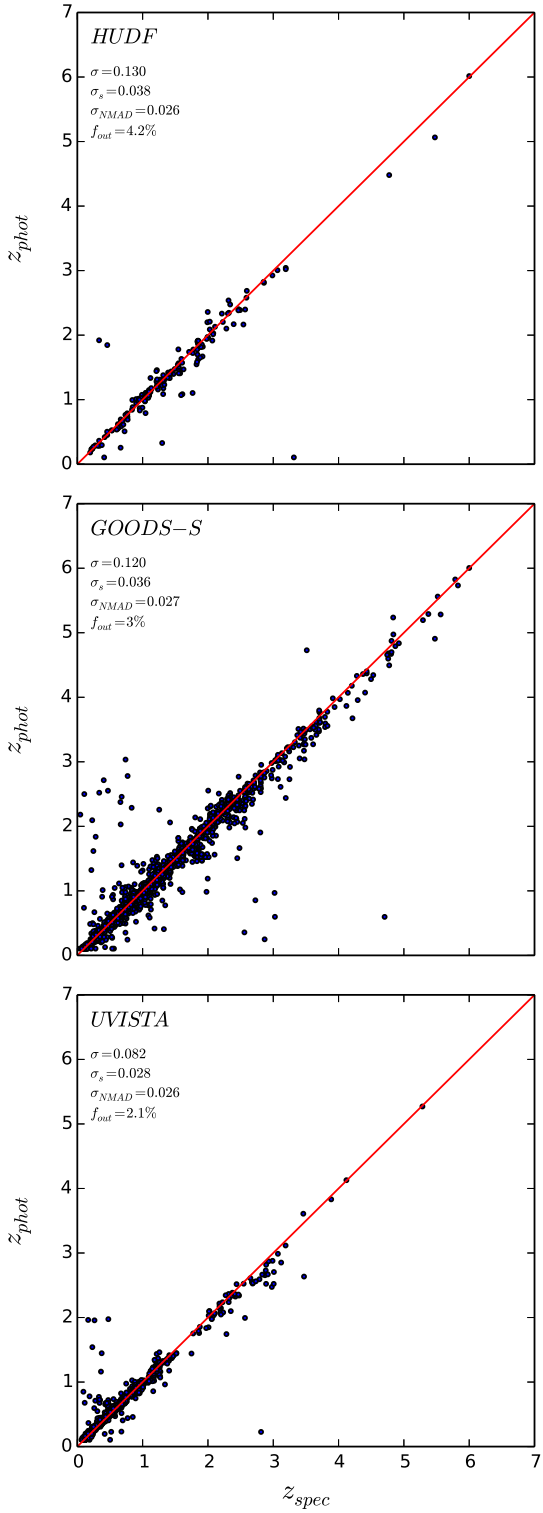

Figure 2. The comparison of our new photometric redshifts versus the high-quality spectroscopic redshifts in each of the three survey fields. The top plot for the *HUDF* contains 210 galaxies, the central plot for CANDELS/GOODS-S contains 2677 galaxies, while the bottom plot for UltraVISTA/COSMOS contains 1671 galaxies. As summarized by the statistics in each panel, the accuracy of our photometric redshifts is comparable with the very best ever achieved for high-redshift galaxy surveys; see Section 3 and Appendix A for further details.

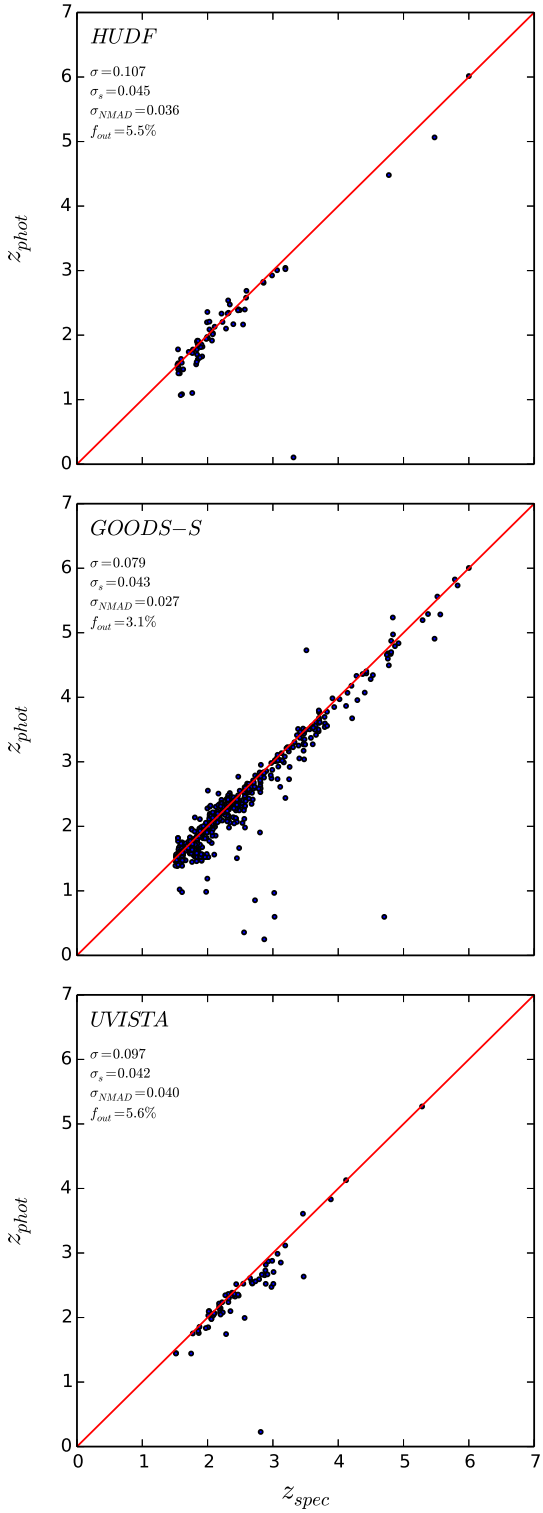

Figure 3. A second comparison of our new photometric redshifts versus the high-quality spectroscopic redshifts in each of the three survey fields, this time confined to $z > 1.5$. The *HUDF* plot contains 72 galaxies, the CANDELS/GOODS-S plot contains 668 galaxies, while the UltraVISTA/COSMOS plot contains 71 galaxies. As summarized by the statistics in each panel, the accuracy of our photometric redshifts remains comparable with the very best ever achieved for high-redshift galaxy surveys; see Section 3 and Appendix A for further details.

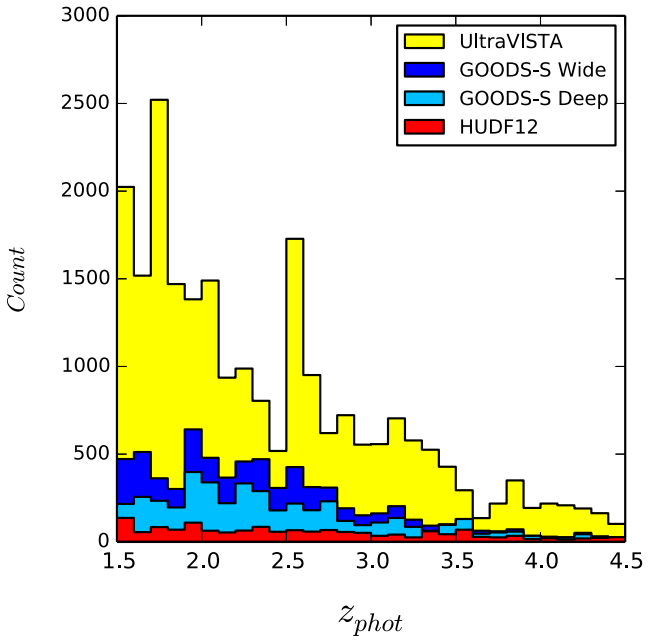

Figure 4. The distribution of photometric redshifts for our final galaxy sample comprising a total of 36 051 galaxies in the redshift range $1.5 < z_{\rm phot} < 4.5$. The different coloured histograms show the redshift distribution subdivided by survey-field/depth, with 1549 galaxies from the *HUDF* with $H_{160} < 29.5$ (red), 4465 galaxies from CANDELS/GOODS-S Deep with $H_{160} < 27$ (cyan), 6947 galaxies from CANDELS/GOODS-S Wide with $H_{160} < 26$ (blue), and 23 090 galaxies from the UltraVISTA/COSMOS field with $i' < 26.0$ (yellow).

For consistency with the *HST HUDF*+GOODS-S data analysis, the photometric redshifts and rest-frame absolute UV magnitudes were then again recomputed using Le Phare with emission lines, yielding acceptable ($\chi^2 < 20$) photometric redshifts for 88 789 galaxies with $i' < 26$ in the UltraVISTA/COSMOS field.

The accuracy of the derived photometric redshifts in UltraVISTA/COSMOS is illustrated in the bottom panel of Fig. 2, which shows $z_{\rm phot}$ v $z_{\rm spec}$ for the 1671 galaxies in the field with secure spectroscopic redshifts, *and* acceptable photometric redshifts. The outlier fraction is only 2.1 per cent, and $\sigma_{\rm NMAD} = 0.026$. For redshifts confined to $z > 1.5$ the $z_{\rm phot}$ v $z_{\rm spec}$ plot is shown in the bottom panel of Fig. 3 (see Appendix A for further details).

3.3 Final galaxy sample

The final galaxy sample consists of 36 051 galaxies selected to lie in the redshift range $1.5 < z < 4.5$, and consists of (i) 1549 galaxies from the *HUDF* with $H_{160} < 29.5$, (ii) 11 412 galaxies from GOODS-S (comprising 4465 from CANDELS/GOODS-S Deep with $H_{160} < 27$ and 6947 from CANDELS/GOODS-S Wide with $H_{160} < 26$), and (iii) 23 090 galaxies from the UltraVISTA/COSMOS field with $i' < 26.0$.

The redshift distributions of these final *HUDF*, CANDELS/GOODS-S and UltraVISTA/COSMOS samples are shown in Fig. 4.

Absolute magnitudes at UV rest-frame wavelengths $\lambda_{\rm rest} = 1500$ and 1700 Å for use in the subsequent LF analyses were computed from the Le phare SED fits using a 100 Å top-hat synthetic filter centred at the appropriate rest wavelength.

4 THE GALAXY LF

Armed with redshifts and absolute UV magnitudes for over 35 000 galaxies in the redshift range $1.5 < z < 4.5$, we can now derive the rest-frame UV galaxy LF, exploring its form and evolution from $z = 2$–4. To aid comparison with previous results in the literature, we derive LFs at both $\lambda_{\rm rest} = 1500$ and 1700 Å as required, but for our final calculations of the evolution of LF parameters, and the evolution of luminosity density (and hence SFR density), we focus on 1500 Å at all redshifts.

In the first subsection, below, we outline the (straightforward) method we have adopted to determine the non-parametric binned form of the LF, and then the parametric form (in this case the Schechter function).

We then present and discuss our results at various redshifts, in part to facilitate comparison with the literature. Specifically, we consider first the UV LF at 1500 Å in the redshift range $1.5 < z < 2.5$ ($z \simeq 2$) (in particular focusing on the faint-end slope, α), before considering separately the 1500 Å LF at $1.5 < z < 2$ ($z \simeq 1.7$) and the 1700 Å LF at $2 < z < 2.5$ ($z \simeq 2.2$). We then move on to determine the evolution of the 1500 Å galaxy LF over the redshift range $z \simeq 1.5$–4.5, in three redshift bins of width $\Delta z = 1$ (i.e. corresponding to $z \simeq 2$, $z \simeq 3$ and $z \simeq 4$).

4.1 Method

Various techniques can be utilized to derive the LF, but here we have sufficiently extensive and dense coverage of the luminosity-redshift plane to obtain a non-parametric estimate by applying the straightforward $V_{\rm max}$ estimator (Schmidt 1968) given by

$$\phi(M){\rm d}M = \sum_i \left[\frac{1}{C(m_i)V_{{\rm max},i}}\right] \quad (1)$$

where the sum is over all galaxies in the given redshift and absolute magnitude bin (chosen here to have a width of $\Delta M = 0.5$ mag), $V_{\rm max}$ for each galaxy is set by the upper redshift limit of the bin unless the source drops out of the sample before that redshift is achieved, and C is the completeness factor for each source. The errors on the derived number density in each bin are here assumed to be Poissonian.

The completeness factor corrects for incompleteness caused both by the fact that significant regions of the imaging are in practice inaccessible for high-redshift object selection (i.e. areas masked due to the presence of bright foreground galaxies or stars/diffraction spikes) and by photometric scatter (which obviously impacts most seriously on the faintest magnitude bins). This has been calculated by Monte Carlo source injection and retrieval simulations, and over most of the magnitude range in each sample transpires to be $\simeq$ 70 per cent in the *HUDF* and CANDELS/GOODS-S fields, and $\simeq$ 60 per cent in the UltraVISTA/COSMOS field.

Obviously, within each of the three survey fields utilized here, incompleteness becomes more serious as the detection limit is approached, and the impact of photometric scatter becomes significant. However, in the present study the impact of this is minimal, as there is sufficient overlap between the regions of the luminosity-redshift plane covered by the different surveys that we can, for example, discard all seriously incomplete faint bins from the UltraVISTA/COSMOS survey in favour of the first well-sampled brighter bins from the CANDELS/GOODS-S survey (and similarly ensuring the LF determination is dictated by the *HUDF* before CANDELS/GOODS-S becomes seriously incomplete). At the very

faint end we neglect all bins delivered by the *HUDF* in which photometric scatter results in a completeness <90 per cent.

Finally, having derived the non-parametric LF from the combination of our three surveys, we fit the binned values with a Schechter function (Schechter 1976):

$$\phi(M) = 0.4ln10\phi^*(10^{-0.4(M-M^*)})^{\alpha+1}e^{-10^{-0.4(M-M^*)}}, \quad (2)$$

where ϕ^*, M^* and α indicate, respectively, the normalization coefficient, the characteristic magnitude and the faint end slope of the LF, and derive confidence intervals on the parameters.

4.2 The galaxy UV LF at $z \simeq 2$

4.2.1 $1.5 < z < 2.5$

We first derive a new measurement of the galaxy rest-frame UV LF at $z \simeq 2$, based on all galaxies in our combined sample with photometric redshifts in the range $1.5 < z < 2.5$. Fig. 5 shows the resulting LF at $\lambda_{\rm rest} = 1500$ Å, including our best-fitting Schechter function. Here, bins brighter than $M_{1500} = -20$ are dominated by the UltraVISTA COSMOS sample, while at the faintest magnitudes the *HUDF* sample allows us to extend the UV LF down to $M_{1500} \simeq -14.5$, which is $\simeq$5 mag fainter than achieved by Oesch et al. (2010). The extension of the $z \simeq 2$ LF to comparably faint magnitudes has only previously been reported by Alavi et al. (2014). However, this was only achieved with the aid of the gravitational lensing provided by the cluster Abell 1689, resulting in very small effective survey volumes and consequently much poorer S/N than achieved here.

The most striking result of our new $z \simeq 2$ LF determination, as shown in the upper panel of Fig. 5, is that we find a much shallower faint-end slope ($\alpha = -1.32 \pm 0.03$) than reported by either Oesch et al. (2010) or Alavi et al. (2014) who found $\alpha = -1.60 \pm 0.51$ and -1.74 ± 0.08, respectively. The lower panel in Fig. 5 shows that an accurate measurement of α requires good sampling of the LF at magnitudes fainter than $M_{1500} \simeq -17$, after which the fitted value of α stabilizes and yields a robust measurement. It is therefore not surprising that Oesch et al. (2010) deduced an erroneously steep faint-end slope given the limited depth of the data utilized in that study.

Our best-fitting values of the other Schechter parameters at $z \simeq 2$ are $M^* = -19.68 \pm 0.05$ and $\phi^* = 7.02 \pm 0.66$ ($\times 10^{-3}$ Mpc^{-3} mag^{-1}). Also shown in Fig. 5 is the $z \simeq 2$ UV LF inferred by Weisz et al. (2014) from Local Group galactic archaeology. Interestingly, it is this 'reverse engineered' LF which agrees best with our new direct determination, as Weisz et al. (2014) also infer a very similar, shallow faint-end slope of $\alpha = -1.36 \pm 0.11$.

4.2.2 $1.5 < z < 2$ and $2 < z < 2.5$

To further facilitate comparison with previous studies, we next compute the UV LF within finer redshift bins, $1.5 < z < 2$ and $2 < z < 2.5$. We calculate the LF in the latter redshift bin at $\lambda_{\rm rest} = 1700$ Å to simplify direct comparison with the results of Reddy & Steidel (2009) and Sawicki (2012), both of whom calculated the LF at 1700 Å based on colour selection sampling an effective redshift window $1.9 < z < 2.7$.

Our results at $z \simeq 1.7$ and $z \simeq 2.2$ are shown in Fig. 6. As in Fig. 5, the upper panels show the binned LF and best-fitting Schechter function, while the lower panels show the derived value of faint-end slope, α, as a function of the absolute magnitude limit down to which the fitting is performed. Again it can be seen that the derived value of α only stabilizes at $M_{\rm UV} > -17$, and that studies reaching only $M_{\rm UV} \simeq -19$ are likely to yield an eroneously steep faint-end slope.

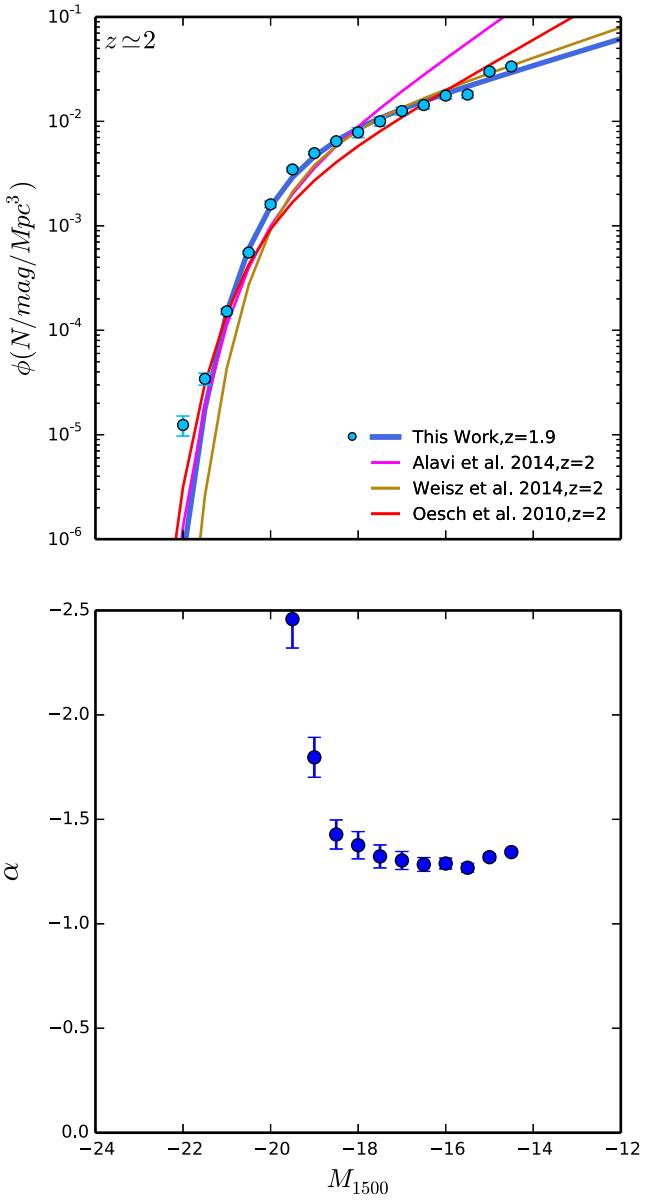

Figure 5. The galaxy rest-frame UV LF at $z \simeq 2$. The upper panel shows the new 1500 Å LF as derived from our combined galaxy sample in the redshift range $1.5 < z < 2.5$. The blue circles with errors indicate the number densities from the $V_{\rm max}$ estimator (see Table 2) and the blue line is our best-fitting Schechter function. The red and pink lines are the Schechter functions at $z \simeq 2$ reported by Oesch et al. (2010) and Alavi et al. (2014), respectively, both of whom derived a much steeper faint-end slope at $z \simeq 2$. The orange line shows the $z \simeq 2$ LF as inferred by Weisz et al. (2014); this has a significantly shallower faint-end slope, in excellent agreement with the value of α deduced from our new determination (see Section 4.2.1). The lower panel shows how the fitted value of α depends on the limiting absolute magnitude down to which the fitting is performed. It can be seen that the derived faint-end slope stabilizes at $M_{1500} > -17$, settling to a secure and robust value of $\alpha = -1.32 \pm 0.03$.

Our derived Schechter parameter values for the 1500 Å LF at $z \simeq 1.7$ are $M^* = -19.61 \pm 0.07$, $\phi^* = 6.81 \pm 0.81$ ($\times 10^{-3}$ Mpc^{-3} mag^{-1}), and $\alpha = -1.33 \pm 0.03$. In the left-hand panel of Fig. 6, we also show the Schechter function derived

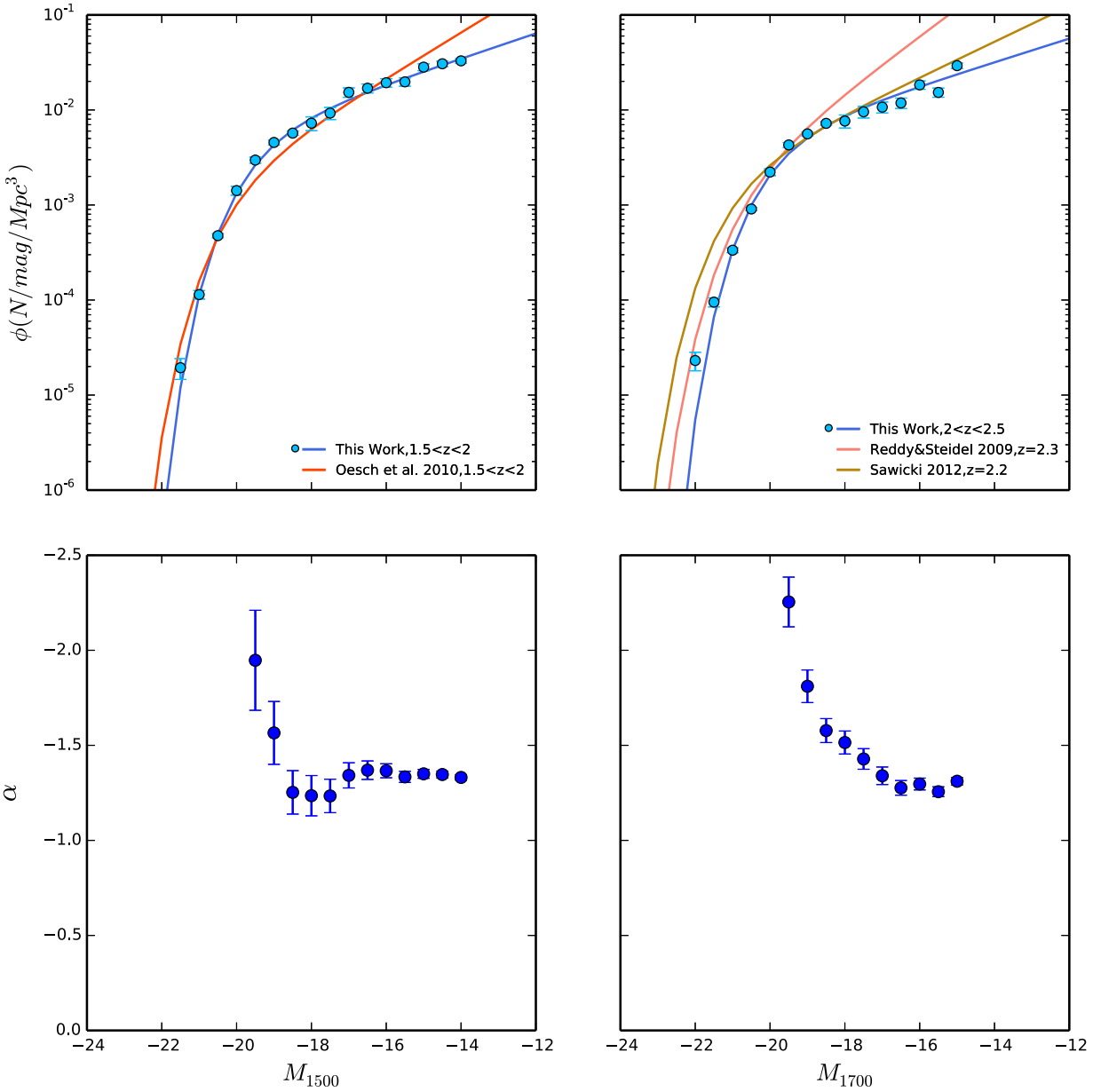

Figure 6. Upper-left: the 1500 Å LF as derived for galaxies in the redshift bin $1.5 < z < 2$. The blue data points show the number densities measured using the $V_{\rm max}$ method and the solid blue line is our best-fitting Schechter function. The yellow solid line with the steeper faint-end slope is the best-fitting Schechter LF measured by Oesch et al. (2010) over the same photometric redshift range. Upper-right: the 1700 Å LF derived over the photometric redshift range $2 < z < 2.5$. Again the blue data points show the binned number densities as derived from the $V_{\rm max}$ method, while the solid blue line is our best-fitting Schechter function. The pink and yellow lines indicate, respectively, the Schechter function LFs derived by Reddy & Steidel (2009) and Sawicki (2012), based on colour selection. The lower panels again show how the fitted value of α depends on the limiting absolute magnitude down to which the fitting is performed.

by Oesch et al. (2010) in the same redshift interval; it can be seen that while the bright end is comparable, Oesch et al. (2010) inferred a much steeper faint-end slope of $\alpha = -1.6 \pm 0.21$.

For the 1700 Å LF at $z \simeq 2.2$ we find $M^* = -19.99 \pm 0.08$, $\phi^* = 6.20 \pm 0.77\,(\times 10^{-3}\,{\rm Mpc}^{-3}\,{\rm mag}^{-1})$, and $\alpha = -1.31 \pm 0.04$. In the right-hand panel of Fig. 6, we also show the Schechter functions derived by Reddy & Steidel (2009) and Sawicki (2012) from very similar redshift ranges. While our LF matches that derived by Reddy & Steidel (2009) around the break, the faint-end slope derived by Reddy & Steidel (2009) was clearly much steeper, with $\alpha = -1.73 \pm 0.07$. The faint-end slope derived by Sawicki (2012) was somewhat shallower (although still steeper than our new derivation), but rather uncertain ($\alpha = -1.47 \pm 0.24$). Moreover, it can also be seen that the bright-end of the LF as derived by Sawicki (2012) also deviates significantly from our new results.

4.3 The galaxy UV LF at $z \simeq 3$ and $z \simeq 4$

We now extend our study of the galaxy UV LF out to higher redshift, considering also the redshift bins $2.5 < z < 3.5$ and $3.5 < z < 4.5$, in order to explore how the LF evolves over the crucial redshift range $z \simeq 2$–4.

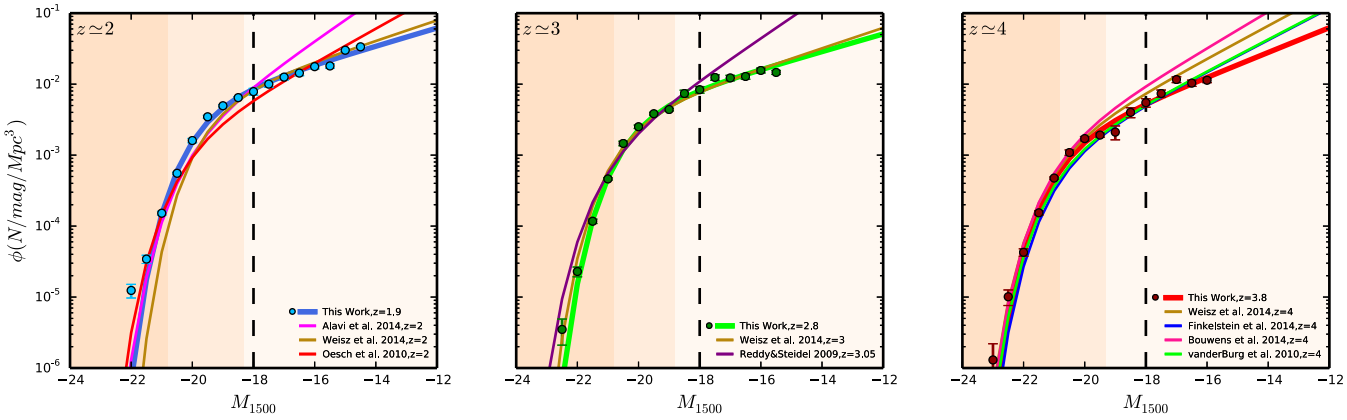

Figure 7. Our new rest-frame UV (1500 Å) galaxy LFs at $z \simeq 2$, 3 and 4. The (blue, green, red) data points indicate the values derived via the V_{max} estimator, with the colour-matched solid lines showing the best-fitting Schechter functions. The values corresponding to the data points and their errors are tabulated in Table 2, while the values of the best-fitting Schechter parameters are given in Table 3, and plotted in Fig. 8. The vertical dashed line in each panel at $M_{1500} = -18$ is shown simply to indicate the typical absolute magnitude limit reached by previous studies at these redshifts, while the background shading indicates the absolute magnitude regimes in which the three different surveys (UltraVISTA/COSMOS, CANDELS/GOODS-S, *HUDF*) make the dominant contribution to our new measurement of the LF at each redshift. For comparison purposes, at each redshift we also show several LFs from the literature as indicated in the legend, and discussed in Section 4.3.

Table 2. The rest-frame UV (1500 Å) galaxy LFs at $z \simeq 2$, 3 and 4, as measured via the V_{max} estimator; these values are plotted in the three panels of Fig. 7, and in Fig. 9.

M_{1500}	ϕ ($z \simeq 2$) (/Mpc^{-3} mag^{-1})	ϕ ($z \simeq 3$) (/Mpc^{-3} mag^{-1})	ϕ ($z \simeq 4$) (/Mpc^{-3} mag^{-1})
−23	–	–	0.000 001 ± 0.000 000
−22.5	–	0.000 003 ± 0.000 001	0.000 010 ± 0.000 002
−22	0.000 012 ± 0.000 027	0.000 023 ± 0.000 004	0.000 043 ± 0.000 005
−21.5	0.000 034 ± 0.000 045	0.000 117 ± 0.000 008	0.000 154 ± 0.000 010
−21	0.000 152 ± 0.000 094	0.000 462 ± 0.000 016	0.000 475 ± 0.000 017
−20.5	0.000 555 ± 0.000 181	0.001 462 ± 0.000 107	0.001 087 ± 0.000 096
−20	0.001 654 ± 0.000 124	0.002 511 ± 0.000 140	0.001 709 ± 0.000 120
−19.5	0.003 467 ± 0.000 165	0.003 830 ± 0.000 173	0.001916 ± 0.000 127
−19	0.004 961 ± 0.000 197	0.004 387 ± 0.000 185	0.002110 ± 0.000 467
−18.5	0.006 454 ± 0.000 225	0.007 382 ± 0.000 838	0.004 008 ± 0.000 644
−18	0.007 849 ± 0.000 869	0.008 353 ± 0.000 892	0.005 485 ± 0.000 753
−17.5	0.010 007 ± 0.000 981	0.012 432 ± 0.001 088	0.007 384 ± 0.000 874
−17	0.012 560 ± 0.001 099	0.012 238 ± 0.001 079	0.016 030 ± 0.001 095
−16.5	0.001 432 ± 0.001 173	0.012 821 ± 0.001 105	0.010 337 ± 0.001 034
−16	0.017 660 ± 0.001 303	0.015 599 ± 0.001 216	0.013 510 ± 0.000 850
−15.5	0.018 052 ± 0.001 317	0.014 625 ± 0.000 971	–
−15	0.030 077 ± 0.001 505	–	–
−14.5	0.033 572 ± 0.001 251	–	–

We have focused on 1500 Å and our results are shown in Fig. 7, alongside the $z \simeq 2$ 1500 Å LF which was shown in Fig. 5. The binned number densities derived from the V_{max} method at $z \simeq 2$, 3 and 4, as shown in Fig. 7, are tabulated in Table 1, and our derived best-fitting Schechter function parameter values at all three redshifts are included in Table 2 (along with various values from the literature, as discussed further in Section 5).

Again, for comparison, in Fig. 7 we also overplot other recent determinations of the 1500 Å LF at these redshifts. Our derived LFs at $z \simeq 3$ and $z \simeq 4$ appear to agree reasonably well with previous measurements around the break luminosity but, as at $z \simeq 2$, we find a shallower faint-end slope, α, than most previous studies; again, we agree best with the results inferred from the local Universe by Weisz et al. (2014) (although we note that, at $z \simeq 3$, Weisz et al. (2014) have adopted the bright end of the 1500 Å LF given by Reddy & Steidel (2009)). At $z \simeq 4$, we find a shallower faint-end slope than most previous studies (i.e. $\alpha = -1.43 \pm 0.04$), but ϕ^* and M^* are in excellent agreement with the results of Bouwens et al. (2014) (see Table 3).

In Fig. 8, we plot our derived Schechter parameter values, with 1σ and 2σ single-parameter confidence intervals, for $z \simeq 2$, $z \simeq 3$ and $z \simeq 4$, while in Fig. 9, we overplot the 1500 Å LFs at these three redshifts. These plots highlight evolutionary trends in the UV LF over this key redshift range, which we discuss further below in Section 5.

5 DISCUSSION AND IMPLICATIONS

5.1 The evolution of the LF from $z \simeq 2$ to $z \simeq 4$

As can be seen in Figs 8 and 9, while the LF displays relatively little evolution between $z \simeq 2$ and $z \simeq 3$, there is a clear drop in ϕ^* (by

Table 3. A compilation of the derived Schechter function parameter values for the UV galaxy LF over the redshift range from $z \simeq 1.7$ to $z \simeq 4.0$, placing the new results derived in this paper in the context of results presented in the literature over the last 10 years. The values tabulated here are included in Fig. 10

Source	z	$\lambda_{\rm rest}$ / Å	M^*	ϕ^*	α
This Work	1.7	1500	-19.61 ± 0.07	$0.006\,81 \pm 0.000\,81$	-1.33 ± 0.03
Oesch et al. (2010)	1.7	1500	-20.17 ± 0.34	$0.002\,34 \pm 0.000\,96$	-1.60 ± 0.21
Sawicki & Thomson (2006)	1.7	1700	-19.80 ± 0.32	$0.016\,98 \pm 0.004\,89$	-0.81 ± 0.21
Hathi et al. (2010)	1.7	1500	-19.43 ± 0.36	$0.002\,17 \pm 0.000\,77$	-1.27 ± 0.00
This Work	1.9	1500	-19.68 ± 0.05	$0.007\,02 \pm 0.000\,66$	-1.32 ± 0.03
Oesch et al. (2010)	1.9	1500	-20.16 ± 0.52	$0.002\,19 \pm 0.001\,23$	-1.60 ± 0.51
Arnouts et al. (2005)	2.0	1500	-20.33 ± 0.50	$0.002\,65 \pm 0.000\,20$	-1.49 ± 0.24
Alavi et al. (2014)	2.0	1500	-20.01 ± 0.24	$0.002\,88 \pm 0.000\,84$	-1.74 ± 0.08
Weisz et al. (2014)	2.0	1500	-19.36 ± 0.28	$0.007\,50 \pm 0.004\,00$	-1.36 ± 0.11
Hathi et al. (2010)	2.1	1500	-20.39 ± 0.64	$0.001\,57 \pm 0.001\,15$	-1.17 ± 0.40
Sawicki & Thomson (2006)	2.2	1700	-20.60 ± 0.38	$0.003\,01 \pm 0.001\,76$	-1.20 ± 0.24
Sawicki (2012)	2.2	1700	-21.00 ± 0.50	$0.002\,74 \pm 0.000\,24$	-1.47 ± 0.24
This Work	2.25	1500	-19.71 ± 0.07	$0.007\,59 \pm 0.000\,88$	-1.26 ± 0.04
This Work	2.25	1700	-19.99 ± 0.08	$0.006\,20 \pm 0.000\,77$	-1.31 ± 0.04
Reddy & Steidel (2009)	2.3	1700	-20.70 ± 0.11	$0.002\,75 \pm 0.000\,54$	-1.73 ± 0.07
Arnouts et al. (2005)	2.7	1500	-21.08 ± 0.45	$0.001\,62 \pm 0.000\,90$	-1.47 ± 0.21
Hathi et al. (2010)	2.7	1500	-20.94 ± 0.53	$0.001\,54 \pm 0.001\,14$	-1.52 ± 0.29
This Work	2.8	1500	-20.20 ± 0.07	$0.005\,32 \pm 0.000\,60$	-1.31 ± 0.04
Arnouts et al. (2005)	3.0	1500	-21.07 ± 0.15	$0.001\,40 \pm 0.000\,00$	-1.60 ± 0.13
Weisz et al. (2014)	3.0	1500	-20.45 ± 0.26	$0.004\,10 \pm 0.002\,00$	-1.36 ± 0.13
Sawicki & Thomson (2006)	3.0	1700	-20.90 ± 0.22	$0.001\,67 \pm 0.000\,13$	-1.43 ± 0.17
van der Burg, Hildebrandt & Erben (2010)	3.0	1600	-20.94 ± 0.14	$0.001\,79 \pm 0.000\,51$	-1.65 ± 0.12
Reddy & Steidel (2009)	3.05	1700	-20.97 ± 0.14	$0.001\,71 \pm 0.000\,53$	-1.73 ± 0.13
This Work	3.8	1500	-20.71 ± 0.10	$0.002\,06 \pm 0.000\,33$	-1.43 ± 0.04
Bouwens et al. (2014)	3.8	1600	-20.88 ± 0.08	$0.001\,97 \pm 0.000\,34$	-1.64 ± 0.04
Bouwens et al. (2007)	3.8	1600	-20.98 ± 0.10	$0.001\,30 \pm 0.000\,20$	-1.73 ± 0.05
Weisz et al. (2014)	4.0	1500	-20.89 ± 0.11	$0.001\,82 \pm 0.000\,10$	-1.58 ± 0.08
Sawicki & Thomson (2006)	4.0	1700	-21.00 ± 0.40	$0.000\,85 \pm 0.000\,21$	-1.26 ± 0.40
van der Burg et al. (2010)	4.0	1600	-20.84 ± 0.09	$0.001\,36 \pm 0.000\,23$	-1.56 ± 0.08
Finkelstein et al. (2015)	4.0	1500	-20.73 ± 0.09	$0.001\,41 \pm 0.000\,21$	-1.56 ± 0.06
Yoshida et al. (2006)	4.0	1500	-21.14 ± 0.14	$0.001\,46 \pm 0.000\,41$	-1.82 ± 0.09

a factor of $\simeq 2.5$) between $z \simeq 3$ and $z \simeq 4$. We also find, however, that M^* brightens steadily over this redshift range, by $\simeq 1$ mag. In terms of luminosity density, this brightening more than offsets the decline in ϕ^* up until $z \simeq 3$, but by $z \simeq 4$ the more dramatic drop in ϕ^* dominates the evolution, and luminosity density undoubtedly declines significantly by $z \simeq 4$.

The modest evolution in ϕ^* and the $\simeq$0.5 mag. brightening in M^* seen between $z \simeq 2$ and $z \simeq 3$ is very similar to the evolution reported by Reddy & Steidel (2009), with the main difference being that our ϕ^* values are systematically higher, and our M^* values systematically dimmer due (at least in part) to our significantly shallower best-fitting faint-end slope α. This is made clear in Fig. 10, where we place our results in the context of several other recent studies. Here, it can be seen that our inferred values of ϕ^* at $z \simeq 2$ and $z \simeq 3$ are noticeably higher than derived in nearly all previous studies, while our inferred values of M^* are therefore (unsurprisingly) somewhat lower. Our results in fact agree best with those recently derived by Weisz et al. (2014), who attempted to reconstruct the form of the UV LF out to $z \simeq 5$ from the properties (including star formation histories) of the galaxies in the Local Group. We speculate that this agreement perhaps reflects the fact that our own study and that undertaken by Weisz et al. (2014) are the only studies to date which have probed to the depths required to properly determine the faint-end slope (in fact Weisz et al. (2014) reach down to $M_{\rm UV} \simeq -5$ at $z \simeq 0$), with an inevitable resulting impact on the inferred best-fitting values of the other two Schechter parameters. While this agreement is interesting, and arguably impressive, we note that, unsurprisingly, the uncertainties in our parameter values are much smaller than those presented by Weisz et al. (2014).

Interestingly, the evolution of ϕ^* and M^* derived here over the redshift range $z \simeq 2$–4, is also very similar to that recently derived for the evolving emission-line galaxy LFs by Khostovan et al. (2015) (although their results were derived by locking the value of the faint-end slope, due to the lack of data of sufficient depth to constrain it).

5.2 Evolution up to $z \simeq 8$

In Fig. 10, we also attempt to place our findings in the wider context of the results derived from a number of recent studies of the UV LF extending out to $z \simeq 8$. It can be seen that the level of agreement is in fact better at $z \simeq 4$ than at $z \simeq 2$ or $z \simeq 3$. The solid black lines in each panel of Fig. 10 show simple parametric fits to the data (i.e. to the published Schechter parameter values), to illustrate the overall evolutionary trend in each parameter as would be derived from the literature. These curves are meant to guide the eye, and are not meant to indicate our best estimate of true parameter evolution; indeed our new, more accurate determinations of ϕ^* and M^* at $z \simeq 2$–3 clearly differ significantly from the literature average (for the well-understood reasons described above). Nevertheless, the evolutionary trend in α indicated by the simple straight-line fit shown in the bottom panel serves to re-emphasize how well our derived shallow faint-end slopes agree with the Weisz et al. (2014)

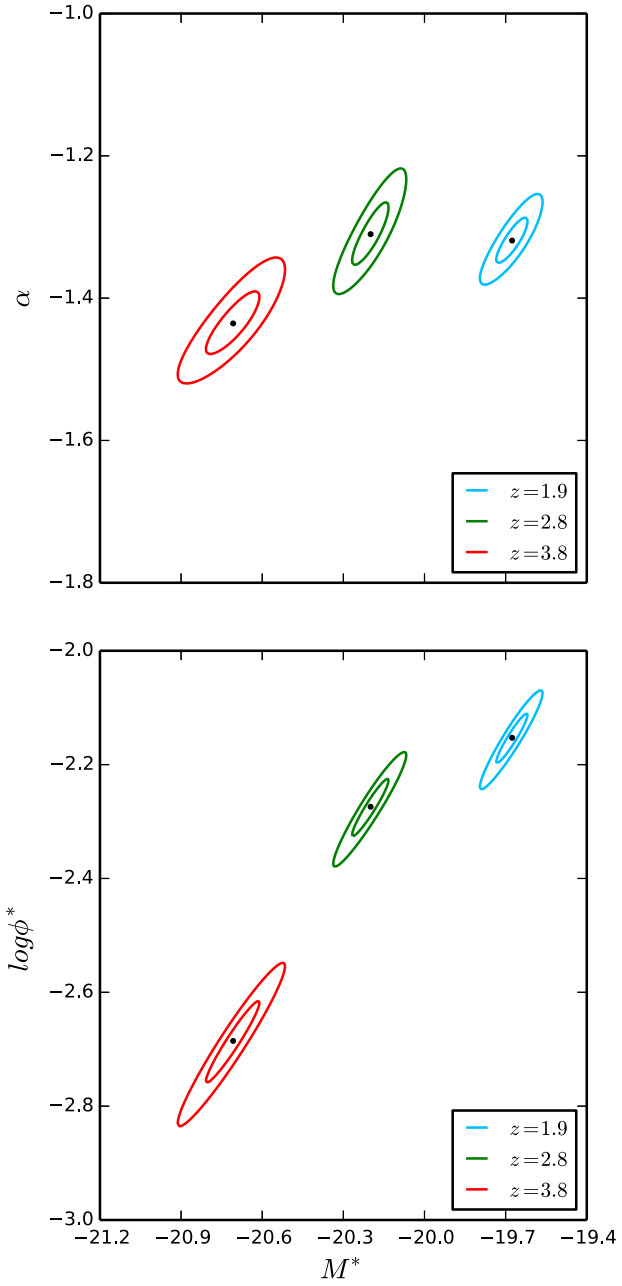

Figure 8. Our derived best-fitting Schechter function parameter values at $z \simeq 2$, 3 and 4, with the associated 1σ and 2σ single-parameter confidence regions (corresponding to $\Delta\chi^2 = 1, 4$ after minimizing over the other parameter). As can be seen from the upper panel, α remains shallow, steepening little if at all over the redshift range. The lower panel shows that ϕ^* drops gradually from $z \simeq 2$ to $z \simeq 3$, but then falls by a factor of $\simeq$2.5 by $z \simeq 4$. However, this drop in number density is offset by a steady brightening in M^* by $\simeq$1 mag. from $z \simeq 2$ to $z \simeq 4$, to the extent that UV luminosity density peaks at $z \simeq 2.5$–3; see Fig. 11.

results, and also shows that such values are in fact in very reasonable agreement with the general trend of a gradual steepening from $\alpha \simeq -1.2$ at $z \simeq 0$ to $\alpha \simeq -2$ by $z \simeq 8$.

5.3 Luminosity density

We finish by considering the evolution of UV luminosity density, $\rho_{\rm UV}$, inferred from our LF determinations over the key redshift

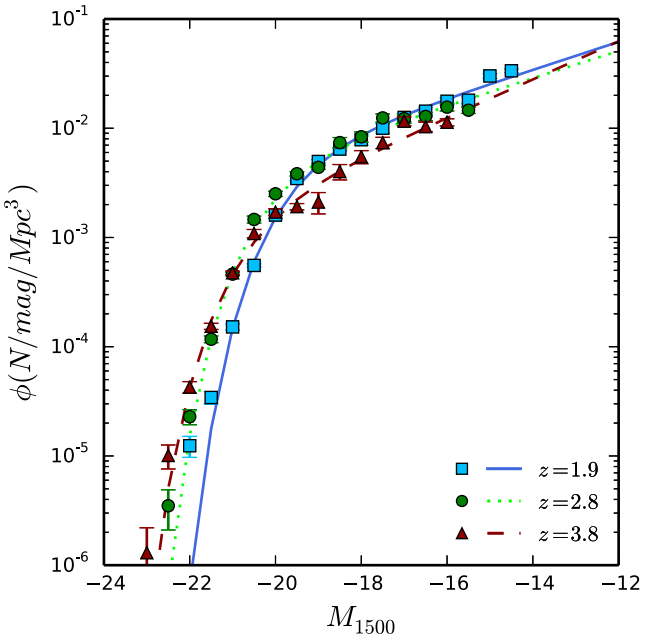

Figure 9. The rest-frame UV (1500 Å) galaxy LFs presented in Fig. 7, now overlaid to show the form of the evolution from $z \simeq 2$ to $z \simeq 4$. As is also clear from the Schechter function parameter values plotted in Fig. 8, it can be seen that (i) the faint-end slope is little changed over this redshift range, (ii) normalization drops only slightly between $z \simeq 2$ and $z \simeq 3$ but then drops by a factor of $\simeq$2.5 by $z \simeq 4$, and (iii) the LF brightens steadily by $\simeq$ 1 mag. from $z \simeq 2$ to $z \simeq 4$.

regime $z \simeq 2$–4. While a full determination of SFR density evolution also requires accounting for the substantial impact of dust obscuration, the luminosity-weighted integral of the UV LF does provide an important measurement of the unobscured SFR density at each redshift.

The results of this calculation are presented in Table 4 and plotted in Fig. 11. Here, we have deliberately performed all calculations using the LFs determined at $\lambda_{\rm rest} = 1500$ Å to enable unbiased comparison of the derived values at each redshift. Table 4 includes results calculated at $z \simeq 2$, 3 and 4, and also provides results for narrower redshift bins at $z \simeq 1.7$ ($1.5 < z < 2.0$) and $z \simeq 2.25$ ($2.0 < z < 2.5$) to enable checking of the trend within the $z \simeq 2$ redshift bin. We also provide results integrated down to different limiting absolute magnitudes: $M_{1500} = -17.7$, $M_{1500} = -15$ and $M_{1500} = -10$. The results to $M_{1500} = -17.7$ are given for ease of comparison with many existing studies, while the convergence seen at the deeper limits shows that, because our derived faint-end slopes are fairly flat, relatively little additional luminosity density is contributed by the faintest galaxies; Fig. 11 shows that $\rho_{\rm UV}$ has essentially converged by $M_{1500} \simeq -15$. Regardless of the chosen integration limit, our results indicate that UV luminosity density (and hence unobscured SFR density) peaks at $z \simeq 2.5$–3, when the Universe was $\simeq 2.5$ Gyr old.

The formal uncertainties indicated by the error bars in Fig. 11 are fairly small, both because the integral of the LF is better constrained than the (somewhat degenerate) Schechter parameters, and because, with such a flat faint-end slope, uncertainties in α only have a minor effect on the luminosity-weighted integral. In practice, therefore, the true uncertainties are likely to be dominated by cosmic variance (although luminosity density is clearly less affected by cosmic variance uncertainties than, for example, bright galaxy number counts).

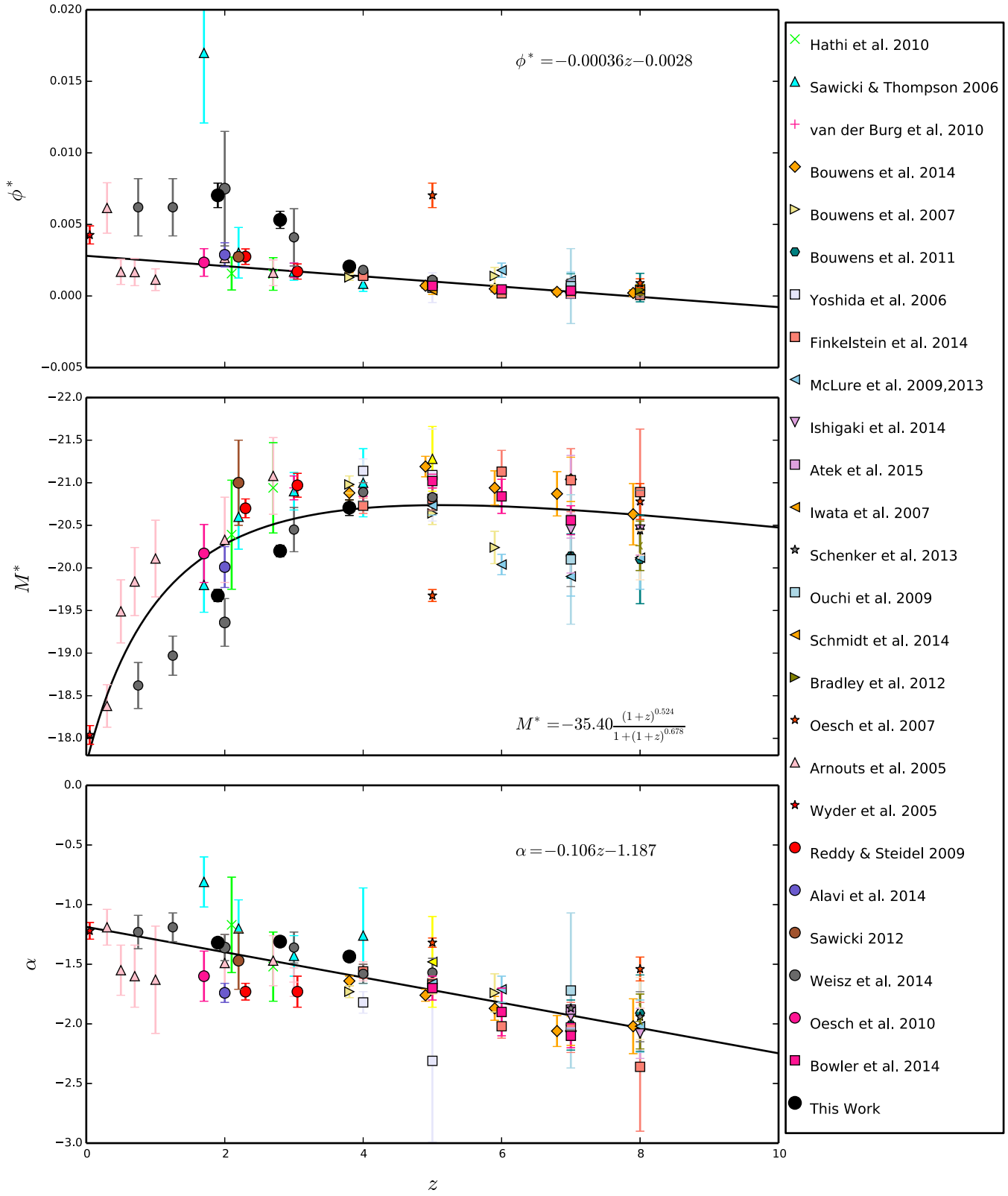

Figure 10. A compilation of the derived Schechter function parameter values for the UV galaxy LF over the redshift range from $z \simeq 0$ to $z \simeq 8$, placing the new results derived in this paper, and the other results tabulated in Table 3, into the wider context of virtually all of cosmic time. Our own results, with error bars (see Fig. 8), are shown by the large black points, with other results from the literature plotted as indicated in the legend. The solid black line in each panel is a simple parametric fit to the data, plotted to illustrate the overall evolutionary trend in each parameter as inferred from the literature. The evolution of ϕ^* and M^* from $z \simeq 2$ to $z \simeq 4$ deduced in the present study is somewhat more dramatic than seen in most pre-existing direct studies of the LF at these redshifts, in fact agreeing best with the values inferred by Weisz et al. (2014) from galactic archaeology of the Local Group. The bottom panel again re-emphasises how well our derived shallow faint-end slopes agree with the Weisz et al. (2014) results, but also shows that such values are in fact in reasonable agreement with the general trend of a gradual steepening from $\alpha \simeq -1.2$ at $z \simeq 0$ to $\alpha \simeq -2$ by $z \simeq 8$.

Table 4. The rest-frame UV (1500 Å) luminosity densities as derived from our UV LFs from $z \simeq 1.7$ to $z \simeq 4$, with the luminosity-weighted integral performed down to three different magnitude limits. Because our derived faint-end slopes are fairly flat, relatively little additional luminosity density is contributed by the faintest galaxies, and Fig. 11 shows that $\rho_{\rm UV}$ has essentially converged by $M_{1500} \simeq -15$. Regardless of the chosen integration limit, it seems clear that UV luminosity density (and hence unobscured star-formation density) peaks at $z \simeq 2.5$–3, when the Universe was $\simeq 2.5$ Gyr old. The values given here are plotted in Fig. 11.

z	$\rho_{\rm UV}/10^{26}$ erg s^{-1} Hz^{-1} Mpc^{-3} $M_{\rm limit} = -10$	$\rho_{\rm UV}/10^{26}$ erg s^{-1} Hz^{-1} Mpc^{-3} $M_{\rm limit} = -15$	$\rho_{\rm UV}/10^{26}$ erg s^{-1} Hz^{-1} Mpc^{-3} $M_{\rm limit} = -17.7$
1.7	2.79 ± 0.04	2.62 ± 0.05	1.91 ± 0.04
1.9	3.01 ± 0.04	2.84 ± 0.06	2.11 ± 0.07
2.25	3.13 ± 0.04	3.00 ± 0.06	2.33 ± 0.07
2.8	3.64 ± 0.01	3.50 ± 0.04	2.86 ± 0.07
3.8	2.70 ± 0.03	2.56 ± 0.05	2.09 ± 0.07

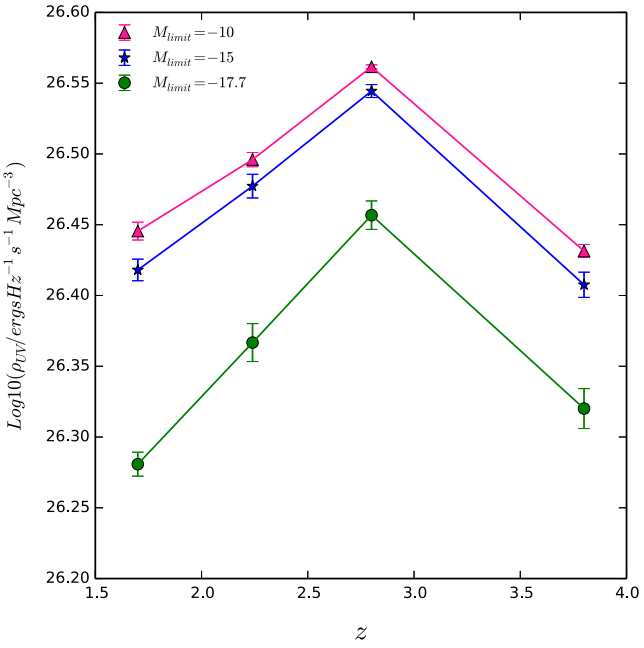

Figure 11. The rest-frame UV (1500 Å) luminosity densities as derived from our UV LFs from $z \simeq 1.7$ to $z \simeq 4$, with the luminosity-weighted integral performed down to three different absolute magnitude limits: $M_{1500} = -17.7$ (green circles), -15 (blue stars) and -10 (pink triangles). The results to $M_{1500} = -17.7$ are shown for ease of comparison with many existing studies, while the convergence seen at the deeper limits shows that, because our derived faint-end slopes are relatively flat, relatively little additional luminosity density is contributed by the faintest galaxies (i.e. the plot shows that $\rho_{\rm UV}$ has essentially converged by $M_{1500} \simeq -15$). Regardless of the chosen integration limit, it seems clear that UV luminosity density (and hence unobscured star formation density) peaks at $z \simeq 2.5$–3, when the Universe was $\simeq 2.5$ Gyr old. The values plotted here are tabulated in Table 4.

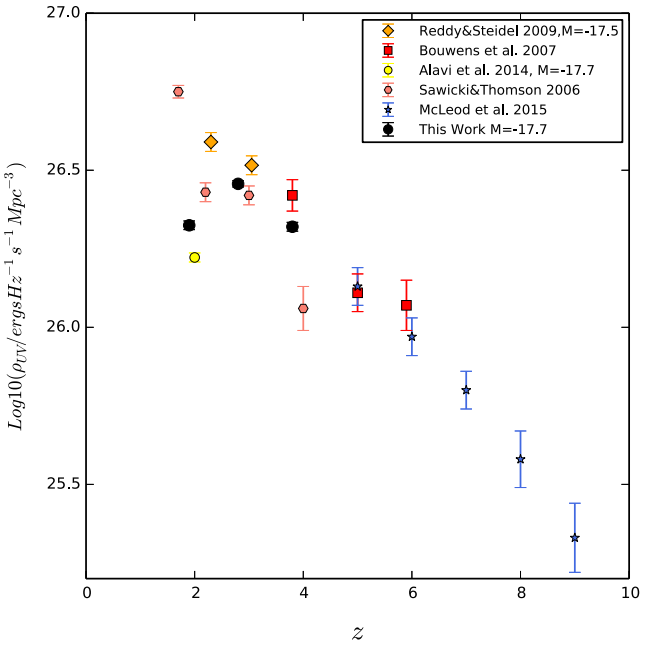

Figure 12. Our derived UV (1500 Å) luminosity density values at $z \simeq 2$, 3 and 4, with integration performed down to $M_{1500} = -17.7$, are here plotted as the black points, and compared to results of similar calculations performed by other authors as indicated in the legend. Our results are more accurate than previous determinations, but in generally good agreement with existing results at $z \simeq 3$ and $z \simeq 4$. At $z \simeq 2$ our new result lies at the low end of the (widely discrepant) previously reported measurements.

Finally, in Fig. 12, we show our derived UV luminosity densities (integrated down to $M_{1500} = -17.7$) in the context of other recent determinations at comparable redshifts, and recent measurements extending to $z \simeq 9$. Our new results are more accurate than previous determinations, but in generally good agreement with existing results at $z \simeq 3$ and $z \simeq 4$. At $z \simeq 2$, our new result lies at the low end of the (widely discrepant) previously reported measurements, but is in fact still higher than the recent estimate provided by Alavi et al. (2014). Even allowing for cosmic variance, the basic conclusion that UV luminosity density peaks at $z \simeq 2.5$–3 appears secure.

Of course, the precise epoch at which cosmic SFR density reached a peak depends on the evolution of the correction for dust obscuration. At $z \simeq 2$, a number of arguments indicate that this correction involves scaling the raw UV luminosity density by a factor of $\simeq$ 4–5 (e.g. Reddy & Steidel 2009; Burgarella et al. 2013; Madau & Dickinson 2014), but whether this correction evolves significantly between $z \simeq 3$ and $z \simeq 2$ remains as yet unclear.

Recent reviews of cosmic star formation history based on data compilations have generally favoured a peak in cosmic SFR density at $z \simeq 2$ (e.g. Behroozi, Weschler & Conroy 2013; Madau & Dickinson 2014) but at least some recent studies (e.g. radio: Karim et al. 2011; far-infrared: Burgarella et al. 2013; emission-line: Khostovan et al. 2015) favour a peak nearer $z \simeq 3$. The latter scenario is more obviously consistent with the new UV results presented here, but a definitive answer awaits more direct measurements of dust-enshrouded star formation at $z \simeq 2$–4 from forthcoming deep

sub-mm/mm surveys with SCUBA-2 on the JCMT and the Atacama Large Millimeter Array.

6 CONCLUSION

We have exploited the high dynamic range provided by combining the *Hubble Ultra Deep Field* (*HUDF*), CANDELS/GOODS-South, and UltraVISTA/COSMOS surveys to derive a new, robust measurement of the evolving rest-frame UV galaxy LF over the key redshift range from $z \simeq 2$ to $z \simeq 4$.

The unparalleled multifrequency photometry available in this survey 'wedding cake', combined with the (relative) wealth of deep optical and near-infrared spectroscopy in these fields, has enabled us to derive accurate photometric redshifts for $\simeq 95$ per cent of the galaxies in the combined survey (with a reliability and accuracy that are competitive with the very best achieved to date, as verified in Appendix A).

This has then enabled us to assemble robust and complete galaxy samples within redshift slices at $z \simeq 2$, 3 and 4, facilitating a new determination of the form and evolution of the UV galaxy LF, that probes $\simeq 3$–4 magnitudes fainter than previous (unlensed) surveys at $z \simeq 2$–3, and does not rely on potentially incomplete colour–colour selection techniques. The SED fitting undertaken to determine the photometric redshifts has also allowed us to determine accurate rest-frame UV absolute magnitudes (M_{1500} or M_{1700}, as required for comparison with previous results).

Our new determinations of the UV LF extend from $M_{1500} \simeq -22$ (AB mag) down to $M_{1500} = -14.5$, -15.5 and -16 at $z \simeq 2$, 3 and 4, respectively. Fitting a Schechter function to the LF data as determined from the $V_{\rm max}$ estimator, at $z \simeq 2$–3 reveals a much shallower faint-end slope ($\alpha = -1.32 \pm 0.03$) than the steeper values ($\alpha \simeq -1.7$) reported by Reddy & Steidel (2009) or by Alavi et al. (2014) (who utilized gravitional lensing to help sample the faint end of the LF). By performing the Schechter function fitting down to differing limiting magnitudes, we show that our measurement of faint-end slope is robust (i.e. the inferred value plateaus/converges at $M_{1500} > -17$). By $z \simeq 4$, the faint-end slope has steepened slightly to $\alpha = -1.43 \pm 0.04$. Although these values are significantly shallower than the aforementioned pre-existing estimates, we find they are in excellent agreement with the values recently inferred by Weisz et al. (2014) (from galactic archaeology of the Local Group), and are in fact consistent with the overall evolutionary trend in α from $z = 0$ to 8, as gleaned from a review of the literature.

Analysis of the other best-fitting Schechter function parameters reveals that our derived number density normalization, ϕ^*, is higher than nearly all previous estimates at $z \simeq 2$ (except, again, Weisz et al. 2014), declines only slightly by $z \simeq 3$, and then drops by a factor of $\simeq 2.5$ to $z \simeq 4$ (where our value agrees well with most previous measurements). Meanwhile, this drop in number density is offset by a steady brightening in M^* by $\simeq 1$ mag. from $z \simeq 2$ to $z \simeq 4$, to the extent that UV luminosity density does not drop significantly until the negative density evolution takes over and dominates beyond $z \simeq 3$.

Finally, we have compared our new UV LF determinations, and the resulting inferred evolution of UV luminosity density ($\rho_{\rm UV}$), with results from a range of previous studies extending from $z \simeq 0$ out to $z \simeq 9$. Because our new measurements yield fairly flat faint-end slopes, our estimates of $\rho_{\rm UV}$ are relatively robust; they have essentially converged by $M_{\rm UV} \simeq -15$, and are little influenced by remaining uncertainties in α. We conclude that unobscured UV luminosity density (and hence unobscured star formation density) peaks at $z \simeq 2.5$–3, when the Universe was $\simeq 2.5$ Gyr old. Whether or not this coincides with the peak in *total* cosmic SFR density ($\rho_{\rm SFR}$) depends on the results of ongoing efforts to determine the level and evolution of dust obscuration at this epochs.

ACKNOWLEDGEMENTS

SP acknowledges the support of the University of Edinburgh via the Principal's Career Development Scholarship. JSD acknowledges the support of the European Research Council via the award of an Advanced Grant, and the contribution of the EC FP7 SPACE project ASTRODEEP (Ref. no: 312725). RJM and AM acknowledge the support of the European Research Council via the award of a Consolidator Grant (PI McLure). This work is based in part on observations made with the NASA/ESA *Hubble Space Telescope*, which is operated by the Association of Universities for Research in Astronomy, Inc., under NASA contract NAS5-26555. This work is also based in part on observations made with the *Spitzer Space Telescope*, which is operated by the Jet Propulsion Laboratory, California Institute of Technology under NASA contract 1407. This work uses data taken with the Hawk-I instrument on the European Southern Observatory (ESO) Very Large Telescope from ESO programme: 092.A-0472. This work is based in part on data products from observations made with ESO Telescopes at the La Silla Paranal Observatories under ESO programme ID 179.A-2005 and on data products produced by TERAPIX and the Cambridge Astronomy survey Unit on behalf of the UltraVISTA consortium. This study was based in part on observations obtained with MegaPrime/MegaCam, a joint project of CFHT and CEA/DAPNIA, at the CFHT which is operated by the National Research Council (NRC) of Canada, the Institut National des Science de l'Univers of the Centre National de la Recherche Scientifique (CNRS) of France, and the University of Hawaii. This work is based in part on data products produced at TERAPIX and the Canadian Astronomy Data Centre as part of the CFHT Legacy Survey, a collaborative project of NRC and CNRS.

REFERENCES

Alavi A. et al., 2014, ApJ, 780, 143
Arnouts S. et al., 2005, ApJ, 619, L43
Ashby M. L. N. et al., 2013, ApJ, 769, 80
Atek H. et al., 2015, AJ, 800, 18
Balestra I. et al., 2010, A&A, 512, 22
Beckwith S. V. W. et al., 2006, AJ, 132, 1729
Behroozi P. S., Silk J., 2015, ApJ, 799, 32
Behroozi P. S., Weschler R. H., Conroy C., 2013, ApJ, 770, 57
Benitez N., 2000, ApJ, 536, 571
Bertin E., Arnouts S., 1996, A&AS, 117, 393
Bouwens R. J., Illingworth G. D., Franx M., Ford H., 2007, ApJ, 662, 72
Bouwens R. J. et al., 2010, ApJ, 709, L133
Bouwens R. J. et al., 2011, ApJ, 737, 90
Bouwens R. J. et al., 2014, ApJ, 795, 126
Bouwens R. J. et al., 2015, ApJ, 803, 34
Bowler R. A. A. et al., 2012, MNRAS, 426, 2772
Bowler R. A. A. et al., 2014, MNRAS, 440, 2810
Bowler R. A. A. et al., 2015, MNRAS, 452, 1817
Bradley L. D. et al., 2012, ApJ, 760, 108
Brammer G. B., van Dokkum P. G., Coppi P., 2008, ApJ, 686, 1503
Bruzual G., Charlot S., 2003, MNRAS, 344, 1000
Burgarella D. et al., 2013, A&A, 554, 70
Calzetti D., Armus L., Bohlin R. C., Kinney A. L., Koornneef J., Storchi-Bergmann T., 2000, ApJ, 533, 682
Cimatti A. et al., 2008, A&A, 482, 21
Cristiani S. et al., 2000, A&A, 359, 489
Croom S. M., Warren S. J., Glazebrook K., 2001, MNRAS, 328, 150

Doherty M., Bunker A. J., Ellis R. S., Mccarthy P. J., 2005, MNRAS, 361, 525
Dunlop J. S., 2013, Astrophys. Space Sci. Libr., 396, 223
Dunlop J. S. et al., 2013, MNRAS, 432, 3520
Ellis R. S. et al., 2013, ApJ, 763, L7
Finkelstein S. L. et al., 2010, ApJ, 719, 1250
Finkelstein S. L. et al., 2015, ApJ, 810, 71
Fioc M., Rocca-Volmerange B., 1999, preprint (astro-ph:9912179)
Fontana A. et al., 2014, A&A, 570, 11
Gerdes D. W., Sypniewski A. J., Mckay T. A., Hao J., Weis M. R., Wechsler R. H., Busha M. T., 2010, ApJ, 715, 823
Giavalisco M. et al., 2004, ApJ, 600, L93
Grogin N. A. et al., 2011, ApJS, 197, 35
Guo Y. et al., 2013, ApJS, 207, 24
Hathi N. P. et al., 2010, ApJ, 720, 1708
Ilbert O. et al., 2006, A&A, 457, 841
Ishigaki M., Kawamata R., Ouchi M., Oguri M., Shimasaku K., Ono Y., 2015, ApJ, 799, 12
Iwata I., Ohta K., Tamura N., Akiyama M., Aoki K., Ando M., Sawicki M., 2007, MNRAS, 376, 1557
Karim A. et al., 2011, ApJ, 730, 61
Kennicutt R. C., Evans N. J., 2012, ARA&A, 50, 531
Khostovan A. A., Sobral D., Mobasher B., Best P. N., Smail I., Stott J. P., Hemmati S., Nayyeri H., 2015, MNRAS, 452, 3948
Koekemoer A. M. et al., 2011, ApJS, 197, 36
Koekemoer A. M. et al., 2013, ApJS, 209, 3
Laidler V. et al., 2007, PASP, 119, 1325
Le Févre O. et al., 2004, A&A, 428, 1043
Lilly S. J., Le Févre O., Hammer F., Crampton D., 1996, ApJ, 460, L1
Lilly S. J. et al., 2007, ApJS, 172, 70
McCracken H. J. et al., 2012, A&A, 544, 156
McLeod D. J., McLure R. J., Dunlop J. S., Robertson B. E., Ellis R. S., Targett T. T., 2015, MNRAS, 450, 3032
McLure R. J., Cirasuolo M., Dunlop J. S., Foucaud S., Almaini O., 2009, MNRAS, 395, 2196
McLure R. J., Dunlop J. S., Cirasuolo M., Koekemoer A. M., Sabbi E., Stark D., Targett T. A., Ellis R. S., 2010, MNRAS, 403, 960
McLure R. J. et al., 2011, MNRAS, 418, 2074
McLure R. J. et al., 2013, MNRAS, 432, 2696
Madau P., 1995, ApJ, 441, 18
Madau P., Dickinson M., 2014, ARA&A, 52, 415
Madau P., Ferguson H. C., Dickinson M. E., Giavalisco M. E., Steidel C. C., Fruchter A., 1996, MNRAS, 283, 1388
Merlin E. et al., 2015, A&A, 582, 15
Mignoli M. et al., 2005, A&A, 437, 883
Morris A. M. et al., 2015, AJ, 149, 178
Nonino M. et al., 2009, ApJS, 183, 244
Oesch P. A. et al., 2007, ApJ, 671, 1212
Oesch P. A. et al., 2010, ApJ, 709, L16
Oesch P. A. et al., 2013, ApJ, 773, 75
Oke J. B., 1974, ApJS, 27, 21
Oke J. B., Gunn J. E., 1983, ApJ, 266, 713
Ouchi M. et al., 2009, ApJ, 706, 1136
Rafelski M. et al., 2015, AJ, 150, 31
Reddy N. A., Steidel C. C., 2009, ApJ, 692, 778
Retzlaff J. et al., 2010, A&A, 511, 50
Riess A. G. et al., 2007, ApJ, 659, 98
Robertson B., Ellis R. S., Dunlop J. S., McLure R. J., Stark D., 2010, Nature, 468, 49
Robertson B. et al., 2013, ApJ, 768, 71
Roche N. D., Dunlop J. S., Caputi K., McLure R., Willott C. J., Crampton D., 2006, MNRAS, 370, 74
Sawicki M., 2012, MNRAS, 421, 2187
Sawicki M., Thompson D., 2006, ApJ, 642, 653
Schechter P., 1976, ApJ, 203, 297
Schenker M. A. et al., 2013, ApJ, 768, 196
Schmidt M., 1968, ApJ, 151
Schmidt K. B. et al., 2014, ApJ, 786, 57
Scoville N. et al., 2007, ApJS, 172, 1
Silverman J. D. et al., 2010, ApJS, 191, 124
Skelton R. E. et al., 2014, ApJS, 214, 24
Strolger L.-G. et al., 2004, ApJ, 613, 200
Szokoly G. P. et al., 2004, ApJS, 155, 271
van der Burg R. F. J., Hildebrandt H., Erben T., 2010, A&A, 523
Vanzella E. et al., 2008, A&A, 478, 83
Weisz D. R., Johnson B. D., Conroy C., 2014, ApJ, 794, L3
Windhorst R. A. et al., 2011, ApJS, 193, 27
Wyder T. K. et al., 2005, ApJ, 619, L15
Yoshida M. et al., 2006, ApJ, 653, 988

APPENDIX A: PHOTOMETRIC REDSHIFT ACCURACY AND RELIABILITY

In this appendix, we provide some additional details on the reliability and accuracy of our photometric redshifts in the three survey fields utilized in this study, and assess how our results compare with other recently published photometric redshift catalogues.

To estimate the accuracy of the photometric-redshift estimation procedure, we compare our photometric redshifts with their spectroscopic counterparts, for the subsamples of galaxies for which high-quality spectroscopic redshifts are known.

Following standard practice, we use the following statistics to quantify the accuracy and reliability of the photometric redshifts.

First, the basic scatter, σ, around the $z_{\rm phot}$: $z_{\rm spec}$ line is defined as

$$\sigma = {\rm rms}[\Delta z/(1+z_{\rm spec})], \tag{A1}$$

where $\Delta z = z_{\rm phot} - z_{\rm spec}$.

Second, 'catastrophic outliers' are defined as galaxies for which

$$|\Delta z|/(1+z_{\rm spec}) > 0.15. \tag{A2}$$

Third, the scatter can be recalculated after exclusion of the catastrophic outliers (in order to estimate the tightness of the core $z_{\rm phot}$: $z_{\rm spec}$ relation); this measure of scatter is usually denoted as $\sigma_{\rm S}$.

Fourth, an alternative measure of scatter, that minimizes the impact of (but does not require the removal of) catastrophic outliers, is the normalized median absolute deviation of Δz defined as

$$\sigma_{\rm NMAD} = 1.48 \times {\rm median}\left(\frac{|\Delta z|}{1+z_{\rm spec}}\right). \tag{A3}$$

As described in Section 3, we have assembled subsamples of galaxies with high-quality spectroscopic redshifts within each of the three fields. In the *HUDF* field, there are 218 such galaxies, and we obtained acceptable photometric redshifts (i.e. $\chi^2 < 50$) for 210 of these. The $z_{\rm phot}$: $z_{\rm spec}$ plot for this subsample of 210 galaxies is shown in the upper panel of Fig. A1, with the normalized redshift error, $\Delta z/(1+z_{\rm spec})$, plotted against $z_{\rm spec}$ shown in the lower panel. The values of the four aforementioned statistics are given in the upper panel. Analogous plots are then shown for the corresponding subsamples of 2677 galaxies in CANDELS/GOODS-S (Fig. A2) and 1671 galaxies in UltraVISTA/COSMOS (Fig. A3). In all three fields, the spectroscopic redhsifts provide coverage from $z \simeq 0$ to at least $z \simeq 5$, and the outlier/scatter statistics are consistent and competitive with the accuracy of the very best photometric redshifts as reported elsewhere in the recent literature; outlier fraction is always significantly lower than 5 per cent, and $\sigma_{\rm NMAD} \simeq 0.026$ in all three fields.

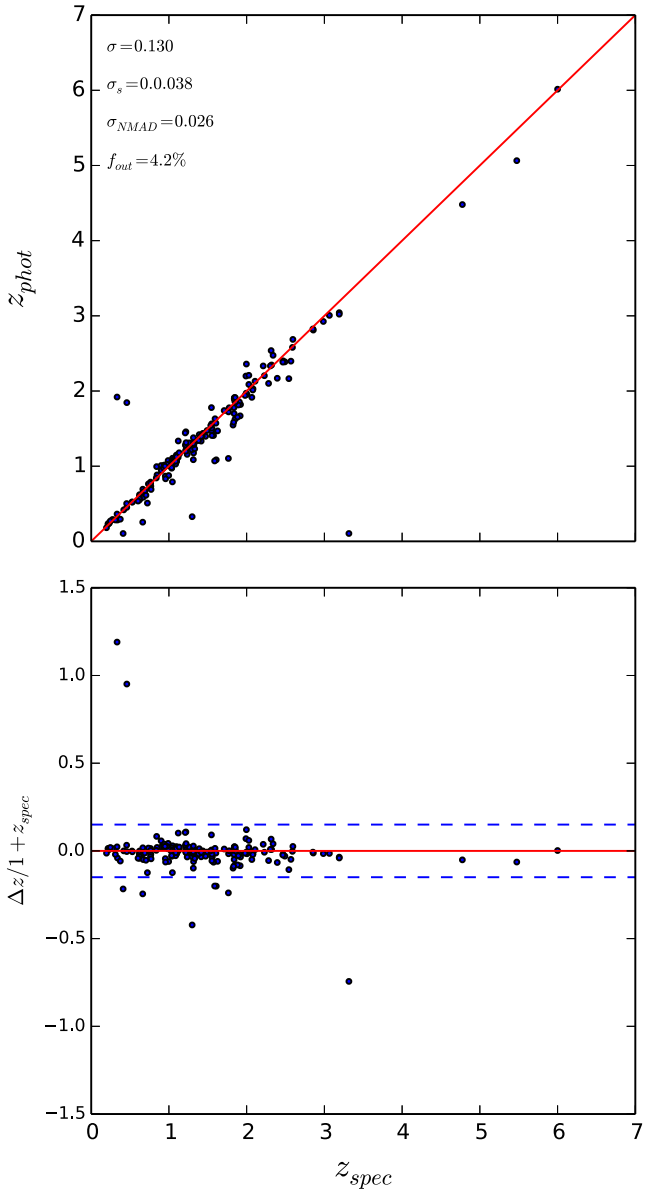

Figure A1. $z_{\rm phot}$ versus $z_{\rm spec}$ for the 210 galaxies in the *HUDF* field with high-quality spectroscopic redshifts and acceptable photometric redshifts ($\chi^2 < 50$). The outlier/scatter measurements are given in the upper panel, while the lower panel redshift error as a function of $z_{\rm spec}$, with the dashed blue lines inidcating the 0.15 boundary used to define the catastrophic outliers.

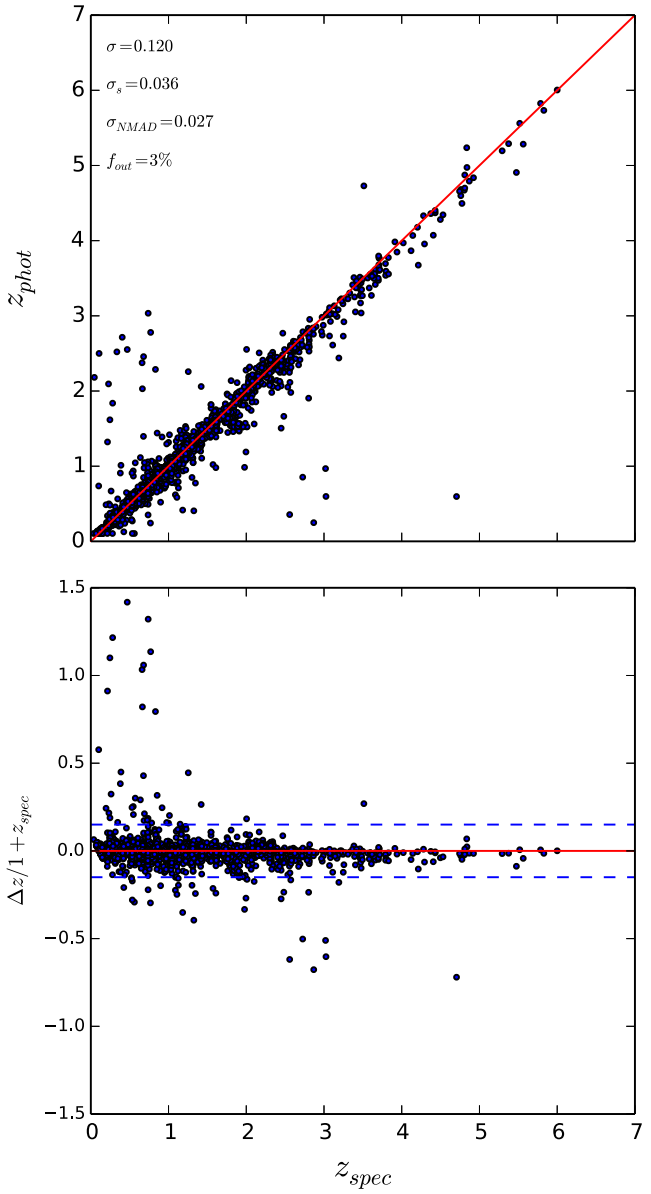

Figure A2. $z_{\rm phot}$ versus $z_{\rm spec}$ for the 2677 galaxies in the CANDELS/GOODS-S field with high-quality spectroscopic redshifts and acceptable photometric redshifts ($\chi^2 < 50$). The outlier/scatter measurements are given in the upper panel, while the lower panel redshift error as a function of $z_{\rm spec}$, with the dashed blue lines inidcating the 0.15 boundary used to define the catastrophic outliers.

Within the CANDELS/GOODS-S field, an alternative set of photometric redshifts has recently been released by the 3D-*HST* team (Skelton et al. 2014). In Fig. A4, we plot our own $z_{\rm phot}$: $z_{\rm spec}$ results for this field (for the same 2677 galaxies shown in Fig. A2) along with the corresponding results as derived from the 3D-*HST* photometric redshift catalogue, and in Table A1, we compare the resulting outlier/scatter statistics. Clearly, these two photometric redshift catalogues are of comparably high quality, although we note that the outlier fraction achieved here is significantly lower, possibly because the 3D-*HST* photometric catalogue does not contain the *HST* *Y*-band imaging. The slightly smaller $\sigma_{\rm NMAD}$ achieved by the 3D-*HST* team appears to result from improved accuracy at low redshifts, possibly driven by their inclusion of medium-band ground-based Subaru imaging. However, at the redshifts of interest in the present study ($z > 1.5$), our own measurements yield a slightly smaller scatter than is achieved by using the 3D-*HST* catalogue.

Similarly, within the *HUDF* field, an alternative set of photometric redshifts has recently been released by Rafelski et al. (2015). In Fig. A5, we plot our own $z_{\rm phot}$: $z_{\rm spec}$ results for this field along with the corresponding results as derived from the Rafelski et al. (2015) photometric redshift catalogue. Here, we are plotting

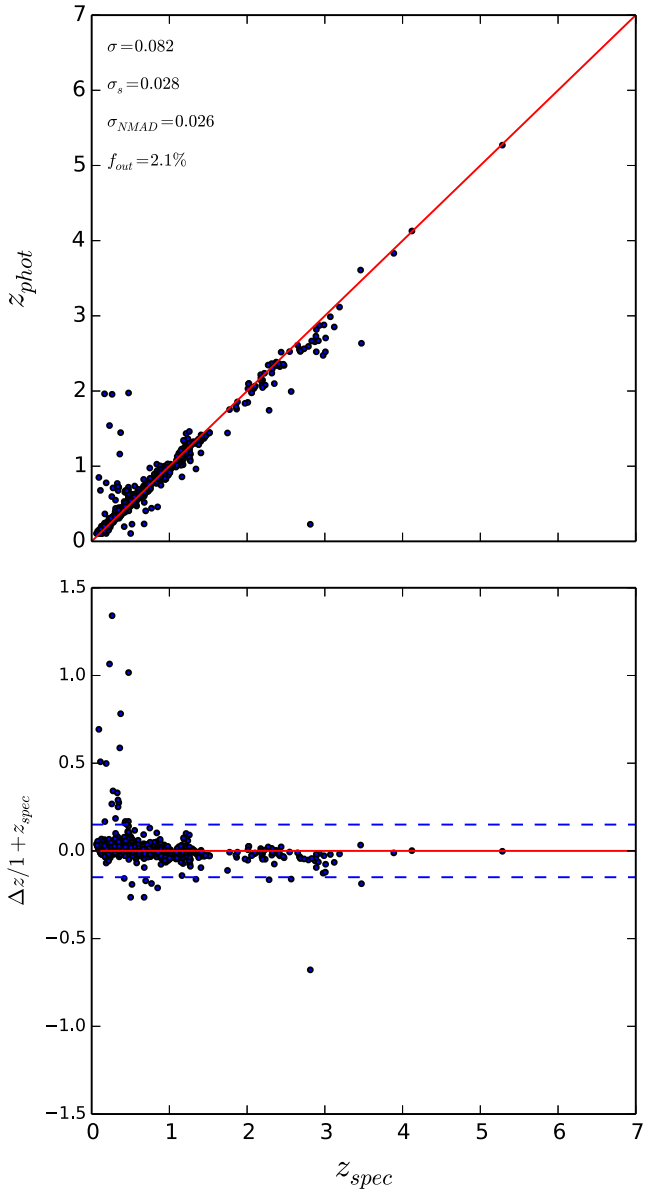

Figure A3. $z_{\rm phot}$ versus $z_{\rm spec}$ for the 1671 galaxies in the UltraVISTA/COSMOS field with high-quality spectroscopic redshifts and acceptable photometric redshifts ($\chi^2 < 20$). The outlier/scatter measurements are given in the upper panel, while the lower panel redshift error as a function of $z_{\rm spec}$, with the dashed blue lines inidcating the 0.15 boundary used to define the catastrophic outliers.

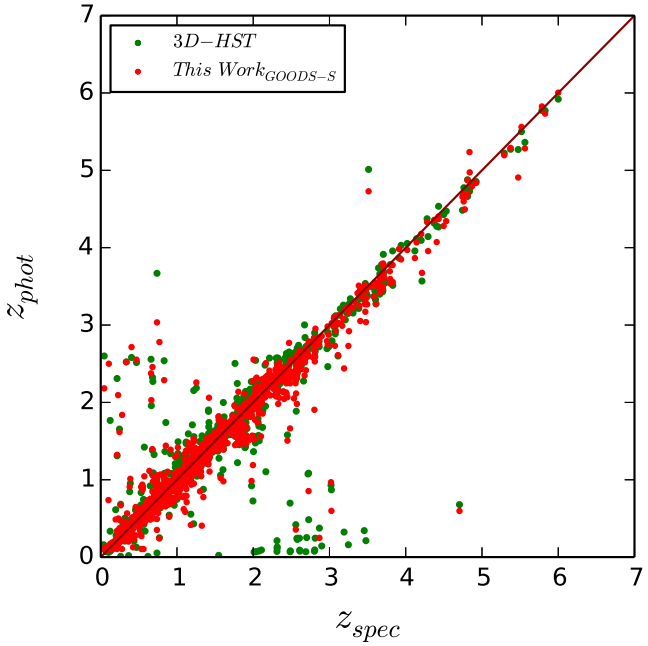

Figure A4. A comparison of the reliability/accuracy of our photometric redshifts in the CANDELS/GOODS-S field with that achieved by the 3D-*HST* team (Skelton et al. 2014). Our results (red points) are overlaid on the results derived from the public catalogue released by the 3D-*HST* team (green points) for the same spectroscopic subsample of 2677 galaxies as previously discussed and presented in Section 3 and Fig. A2. Outlier fractions and scatter statistics are summarized in Table A1, and discussed in the text.

Table A1. The reliability and accuracy of the photometric redshifts for galaxies in the CANDELS/GOODS-S field, as achieved here (see Section 3) and alternatively by utilizing the public 3D-*HST* photometric redshift catalogue (Skelton et al. 2014). σ, $\sigma_{\rm NMAD}$ and $f_{\rm out}$ (see text) have been calculated for the high-quality spectroscopic subsample of 2677 galaxies (see Fig. A4). Our own results yield a lower outlier fraction, possibly because the 3D-*HST* photometric catalogue does not contain the *HST Y*-band imaging. The slightly smaller $\sigma_{\rm NMAD}$ achieved by the 3D-*HST* team appears to result from improved accuracy at low redshifts, possibly driven by their inclusion of medium-band ground-based Subaru imaging. However, at the redshifts of interest in the present study ($z > 1.5$), our own measurements yield a slightly smaller scatter than is achieved by using the 3D-*HST* catalogue.

Group	σ	$\sigma_{\rm S}$	$\sigma_{\rm NMAD}$	$f_{\rm out}$
This Work	0.120	0.036	0.027	3.0 per cent
3D-*HST*	0.135	0.027	0.013	4.3 per cent

results for 207 galaxies (because three of the 210 galaxies plotted in Fig. A1 do not have photometric redshifts in the Rafelski et al. (2015) catalogue). We also include the results from both of the alternative redshift estimation techniques used by Rafelski et al. (2015), which are based on the Bayesian Photometric Redshift (BPZ; Benitez 2000) and Easy and Accurate $z_{\rm phot}$ from Yale (EAZY; Brammer, van Dokkum & Coppi 2008) algorithms. The forme uses a set of Pegase SED models which have been recalibrated based on observed photometry and spectroscopic redshifts from the FIREWORKS catalogue; emission lines are included and LFs observed in COSMOS, GOODS-MUSIC, and the UDF are used as priors. The latter method uses the default EAZY SEDs, with emission lines again included. In Table A2, we again compare the resulting outlier/scatter statistics. Despite the fact that the Rafelski et al. (2015) results include new WFC3/UVIS photometry, again it can be seen that all three sets of results are competitive (presumably because our own calculations utilize the VIMOS *U*-band ground-based photometry, minimizing the additional impact of the new UVIS data). Indeed, our outlier fraction is lower than yielded by the Rafelski et al. (2015) EAZY results which, as in our own calculations, avoid the use of LF priors, and our catalogue yields the lowest value of $\sigma_{\rm NMAD}$.

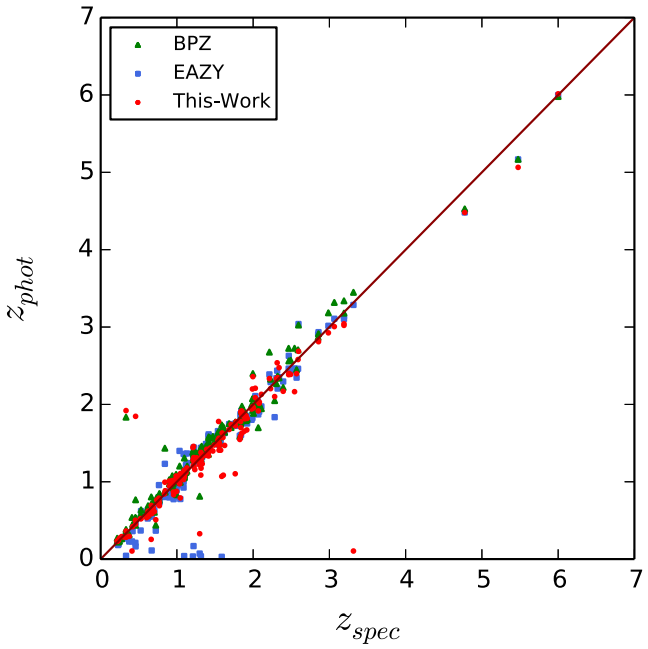

Figure A5. A comparison of the reliability/accuracy of our photometric redshifts in the *HUDF* field with that achieved by the Rafelski et al. (2015). Our results (red points) are overlaid on the results derived using the BPZ (green triangles) and EAZY (blue triangles) algorithms by Rafelski et al. (2015) for 207 of the 210 galaxies in the *HUDF* spectroscopic subsample as previously discussed and presented in Section 3 and plotted in Fig. A1. Outlier fractions and scatter statistics are summarized in Table A2, and discussed in the text.

Table A2. The reliability and accuracy of the photometric redshifts for galaxies in the *HUDF*, as achieved here (see Section 3) and alternatively by utilizing the the new public photometric redshifts released by Rafelski et al. (2015). σ, $\sigma_{\rm NMAD}$ and $f_{\rm out}$ (see text) have been calculated for 207 of the galaxies with high-quality spectroscopic redshift in the *HUDF* (see Fig. A5). Our own results produce a lower outlier fraction than yielded by the Rafelski et al. (2015) EAZY results which, as in our own calculations, avoid the use of LF priors. Moreover, our catalogue yields the lowest value of $\sigma_{\rm NMAD}$.

Algorithm	σ	$\sigma_{\rm S}$	$\sigma_{\rm NMAD}$	$f_{\rm out}$
BPZ	0.093	0.038	0.033	2.4 per cent
EAZY	0.108	0.043	0.033	6.3 per cent
This Work	0.131	0.037	0.026	4.3 per cent

This paper has been typeset from a TEX/LATEX file prepared by the author.